2009-08-11

Real-Time Virus Analysis Via Image Charge Detection Surface Induced Dissociation Tandem Mass Spectrometry

Seth T. Call
Brigham Young University - Provo

Real-Time Virus Analysis via Image Charge Detection

Surface Induced Dissociation Tandem Mass Spectrometry

by

Seth Call

A thesis submitted to the faculty of

Brigham Young University

in partial fulfillment of the requirements for the degree of

Master of Science

Department of Chemistry and Biochemistry

Brigham Young University

December 2009

BRIGHAM YOUNG UNIVERSITY

GRADUATE COMMITTEE APPROVAL

of a thesis submitted by

Seth Call

This thesis has been read by each member of the following graduate committee and by majority vote has been found to be satisfactory.

Date	Daniel Austin, Chair
Date	Matthew Asplund
Date	David Dearden
Date	Randall Shirts

BRIGHAM YOUNG UNIVERSITY

As chair of the candidate's graduate committee, I have read the thesis of Seth Call in its final form and have found that (1) its format, citations, and bibliographical style are consistent and acceptable and fulfill university and department style requirements; (2) its illustrative materials including figures, tables, and charts are in place; and (3) the final manuscript is satisfactory to the graduate committee and is ready for submission to the university library.

Date	Daniel Austin Chair, Graduate Committee

Accepted for the Department

Date	Paul Farnsworth

Accepted for the College

Date	Thomas W. Sederberg, Associate Dean College of Physical & Mathematical Sciences

ABSTRACT

Real-Time Virus Analysis via Image Charge Detection

Surface Induced Dissociation Tandem Mass Spectrometry

Seth Call

Department of Chemistry and Biochemistry

Master of Science

This thesis reports on the development of a novel mass spectrometer combining image charge detection with surface induced dissociation for real-time analysis of intact viruses. Protonated viruses produced using electrospray are accelerated and subsequently impact on a solid surface. Capsid peptides released during the impact are analyzed using time-of-flight mass spectrometry. Image charge detection is used to measure the mass and charge states of structurally intact, electrosprayed viruses prior to impact. Since virus capsids are composed of loosely-bound proteins, collision of viruses with surfaces at moderate impact energies could release intact proteins. The masses and numbers of different protein types combined with the mass of the intact virus represent a unique signature useful for accurate, real-time virus identification.

The progress of instrumentation developed thus far is reported. Techniques were developed for electrospraying intact viruses, including electrospray capillaries with small tips and methods for achieving complete desolvation. Significant reduction of low-frequency and other noise was achieved in the image charge detector as well as determination of accurate methods for mass and charge measurement. Improved focusing and transmission efficiency was achieved via an aerodynamic lens. Suitable surfaces were also obtained including conductive diamond and fluorinated self-assembled monolayer (SAM) surfaces.

ACKNOWLEDGEMENTS

I wish to thank Dr. Daniel Austin for coming up with the idea for this project and for his experience in the design and implementation of the instrument. I wish to thank other members of the group for their tireless support including Terik Daly, Ying Peng, and Zhiping Zhang. I also wish to thank David Dearden for contributing his excellent experience with electrospray and mass spectrometry, as well as Matthew Asplund and Randall Shirts for their input concerning theoretical aspects of the project. I also wish to thank Bart Whitehead for his electrical engineering expertise and Bruce Jackson for his helpful, practical advice with electrospray and mass spectrometry.

Seth Call

CONTENTS

LIST OF TABLES

LIST OF FIGURES

CHAPTER 1

REVIEW OF MASS SPECTROMETRY AND SURFACE INDUCED DISSOCIATION AS RELATED TO VIRUS DETECTION

1.1 Introduction

Mass spectrometry (MS) is an analytical technique for determining the elemental composition and bonding pattern of complex molecules. It is used to analyze simple molecules containing only a few atoms and also many-atom molecules such as proteins. The components of a mass spectrometer include an ion source, a mass analyzer, and a detector. Ion sources create negatively or positively charged sample molecules (ions) and sometimes also fragment the sample. Mass analyzers separate ions based on their mass-to-charge ratio. Detectors then count the number of ions of different mass-to-charge ratios producing a mass spectrum.

Tandem mass spectrometry uses multiple stages of MS by selecting sample ions with a particular mass-to-charge ratio, performing additional fragmentation of these ions, and measuring the mass-to-charge ratios of the sub-fragments.[18,26,54,83] These sub-fragments are referred to as product or daughter ions, and the ion from which they originated is referred to as the precursor or parent ion. Tandem MS instruments can be performed with multiple stages in space or time. Tandem MS in space involves the physical separation of MS stages, and separation in time requires storing ions in an ion trap between MS stages. Tandem MS is used to analyze large, complex molecules that require multiple rounds of fragmentation for chemical analysis. A peptide sequence tag resulting from a peptide tandem mass spectrum is used to identify peptides in a protein database.[70]

In-source fragmentation occurs when a sample is first ionized. Post-source fragmentation is used between MS stages. The most-used post-source fragmentation method is collision induced dissociation (CID),[54,83,102] in which the sample collides with multiple neutral gas molecules. Another method is surface induced dissociation (SID), in which the sample collides with a surface. SID has some advantages over CID. First, surfaces have a greater mass than gas molecules, enabling SID to provide more single-step energy for fragmentation.[104] Second, with SID the energy is provided in a few picosecond,[37,42,54] while CID requires multiple collisions that slowly heat the sample. This slow heating provides time for energy in excited vibrational states to be redistributed, resulting in bond rearrangements and competitive fragmentation pathways[29,104] that create problems in the analysis. Third, with SID the amount of energy transferred to the sample has a much narrower distribution than with CID, since CID cannot tightly control the number of collisions.[29,37,104] Also, SID is beneficial for protein analysis because it can differentiate leucine from isoleucine and glutamine from lysine by varying the amount of kinetic energy of the sample prior to surface collision, something not possible with CID.[21,29,37,54,83,104]

In addition, ion/surface collisions make possible experiments that cannot be performed with CID. For example, viruses are one type of large biomolecule with capsids composed of multiple proteins loosely bound together. Previous studies show that whole, intact viruses can be ionized and weighed with electrospray ionization mass spectrometry.[13,27,34,35,58,82,89,92] The weak-weak interactions between proteins suggests that collisions of ionized viruses with surfaces can provide additional structural information. The type of surface/virus interaction depends on the type of virus, its size and shape, its

velocity, and the surface. Some possible virus/surface interactions[37] as a function of velocity are indicated in Figure 1.

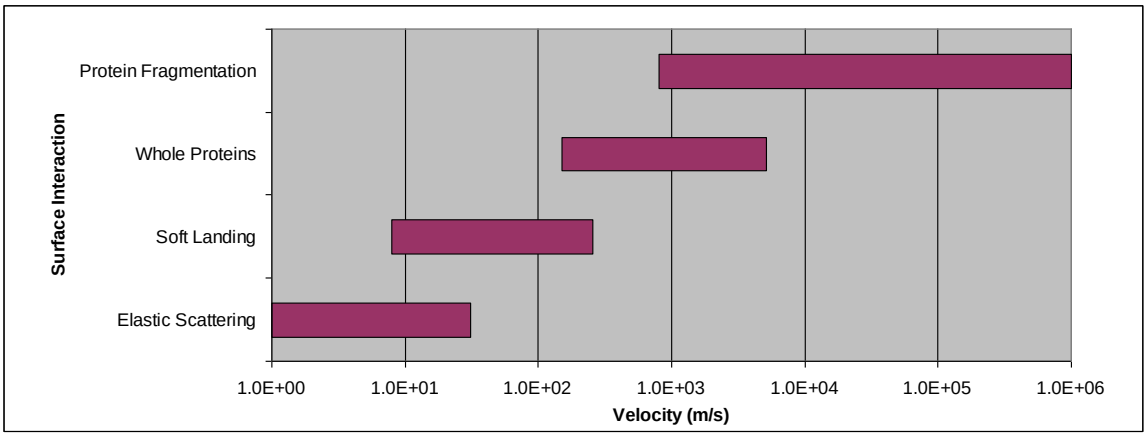

Figure 1. Possible virus/surface interactions at different impact velocities.

Charged viruses can undergo elastic scattering in which they bounce off the surface with no permanent change in virus capsid structure. They can undergo soft landing in which they adsorb to the surface. The weak-weak interactions between protein subunits can be broken, producing whole protein fragments. At higher velocities, covalent bonds within the proteins themselves can break. Production of whole proteins fragments is particularly useful. For example, many viruses are composed of multiple protein types each with a different mass and number of proteins. These protein masses and number ratios provide structural information about the virus and represent a unique signature useful for accurate, real-time virus identification. Such an experiment is best done with a method like SID that can provide more single-step collision energy in a much shorter time and that produces a narrower distribution of kinetic energies.

This report discusses a novel SID mass spectrometer capable of analyzing large biomolecules including viruses. This instrument produces intact, ionized samples via

electrospray ionization and performs an initial mass and charge measurement using image charge detection.[11,13,33,34,35,59,66,77,79,91,108,109] The sample then collides with a surface and the mass-to-charge ratios of the released peptides are analyzed with a time-of-flight mass spectrometer. This research is a form of tandem MS in that two mass-to-charge measurements are made with fragmentation between measurements. It differs from traditional tandem MS in that it does not seek to determine the elemental composition and bonding pattern of complete molecules by breaking covalent bonds. It instead seeks to identify masses of whole proteins contained within virus capsids. In addition, the first mass-to-charge measurement is not preceded by fragmentation, which is often the case with tandem MS. This research also differs in its use of image charge detection, which can measure the mass-to-charge ratios of very massive, highly-charged samples. This overcomes the limitations many MS instruments have in analyzing high-mass, highly charged molecules.[13,34, 35]

This first chapter reviews literature on general techniques in tandem mass spectrometry with an emphasis on SID. The second chapter discusses current methods for virus detection and reviews previous studies where whole viruses were analyzed using mass spectrometry. The third chapter discusses the instrument itself, with an emphasis on design decisions, and how problems were overcome during its construction. The fourth chapter summarizes the performance of the instrument.

1.2 Ion Sources

The first component of a mass spectrometer is the ion source. Ion sources produce gas-phase ions from solid, liquid, and gas-phase samples. Hard ionization processes make unstable products that fragment into product ions, whereas soft ionization techniques produce little or no fragmentation. Ionization methods typically used with gas-phase samples include electron ionization and chemical ionization. With the hard electron ionization or electron impact method, an electron passing through the sample knocks off an additional electron from the sample, producing a radical cation. In the softer chemical ionization method, sample ions are produced via collision with reagent gas plasma molecules, typically methane, ammonia, or isobutene cations.

Ionization methods typically used with liquid or solid samples include Matrix-Assisted Laser Desorption/Ionization (MALDI) and Electrospray Ionization methods, both of which are soft ionization methods. The use of MALDI is quite common and was considered for this experiment. In MALDI,[73] the analyte is added to a matrix solution prepared from crystallized molecules and often an organic solvent such as acetonitrile and high purity water. The three typically used crystallized molecules are 3,5-dimethoxy-4-hydroxycinnamic acid (sinapinic acid), α-cyano-4-hydroxycinnamic acid (alpha-cyano or alpha-matrix) and 2,5-dihydroxybenzoic acid (DHB). The analyte is added to this matrix, spotted on a metal plate, and the solvent evaporates leaving a re-crystallized matrix-analyte mixture. Ionization is triggered with an ultraviolet or near infrared laser, creating ionized analyte molecules. The performance of MALDI depends on many factors. First, the matrix must dissolve the analyte and must be able to transfer charge to the analyte during the ionization process. Also, choosing a matrix that will absorb the

laser light is important. Second, inorganic salts that are often part of protein extracts can interfere with analyte ionization. While these salts can often be removed via washing or solid phase extraction, these methods can also remove other components in the analyte. Third, the type of laser and manner in which it is used also affect results. The laser frequency, pulse width, and incident angle affect MALDI's performance. Moving the position of the laser after each pulse is also necessary for quantitative analysis. Although MALDI has been used for analysis of large biomolecules including viruses,[90] it was not chosen for this experiment since it requires significant amounts of sample. Previous studies also show that electrospray ionization is well suited for ionizing whole, viruses in an intact form.[13,27,34,35,58,82,89,92]

Electrospray Ionization (ESI) is a widely used ionization technique in proteomics and drug discovery because it is a universally-applicable, soft-ionization technique. In ESI,[23,28,41,44,45,47,66,85] analytes are first dissolved in a solvent composed of water and a volatile organic compound such as methanol or acetonitrile. To better enable the solvent to carry positive charge, the pH of the solution is often reduced with an organic acid such as trifluoroacetic acid (TFA). This mixture is pumped through a needle, often composed of a conductive material, which is placed a short distance from the target. A high, usually positive, voltage is applied to the needle, and as the liquid reaches the end, micron-sized, charged droplets form and spray toward the target. The spray is cone-shaped and is called a Taylor cone. High-flow-rate applications also often evaporate solution from electrospray droplets via an inert, heated nebulizing gas such as N_2. As electrospray droplets enter the vacuum chamber, some setups require that they pass through a capillary that can be heated to further desolvate electrospray droplets.

As with MALDI, the electrospray process itself has not been fully explained. Two theories seeking to describe the process are (1) the charged residue model (CRM)[23,28] and the newer (2) ion evaporation model (IEM).[23,41] According to CRM, as solvent evaporates from an electrospray droplet, the charge on the droplet remains. When evaporation produces a sufficiently small droplet, the charge decreases the surface tension until the Rayleigh limit is reached. When this happens, the droplet becomes unstable, deforms, and emits charged jets in a process known as Rayleigh fission. Cycles of evaporation and fission continue until the remaining droplets have at most one analyte molecule per droplet. Evaporation leaves charged analyte particles with the same charge as their parent droplets. CRM predicts high charge states for analyte molecules. High numbers of charges are important for virus detection, with one charge per peptide being desired for *m/z* measurements. The theory of IEM is similar, except it is more applicable to very small analyte molecules. In this theory, it is not until droplets reach a small radius, $R < 10$ nm, that the ion evaporation process becomes dominant.

Two problems with electrospray are nozzle clogging and ion suppression. Nozzle clogging accompanies the use of small tips necessary for reducing initial electrospray droplet sizes. Ion suppression is a reduction or elimination of ionization due to contaminants in the solvent. Research suggests[47] that contaminants may increase the surface tension and/or the boiling point of the solvent which could decrease solvent evaporation efficiency and inhibit offspring droplet formation.

1.3 Mass Analyzers

The second component of a mass spectrometer is the mass analyzer. Mass analyzers separate ions based on their mass-to-charge ratio (*m/z*) using electric or magnetic fields. The motion of particles can be described using the Lorentz force law and Newton's Second law:

$$\vec{F} = q(\vec{E} + \vec{v} \times \vec{B}) = m\vec{a} = m\frac{d^2\vec{x}}{dt^2} \quad (1)$$

where were *F* is the force on the particle, *q* is particle charge, *E* is the electric field, *v* is the particle velocity, *B* is the magnetic field, *m* is mass, and *a* is acceleration.

Some common types of mass analyzers include magnetic sector, time-of-flight, quadrupole, and Fourier transform ion cyclotron resonance, and ion traps. Magnetic sector mass analyzers[15] bend the trajectory of ions using magnetic fields, and then select ions with a particular mass-to-charge (*m/z*) ratio or scan through ions with a range of *m/z* ratios. Time-of-flight instruments[7,60,61] accelerate all ions through the same electric field. Their kinetic energy after acceleration through this field is given from the conservation of energy and the definition of voltage ($V \equiv U/q$) as:[49]

$$U = qV = \frac{1}{2}mv^2 \quad (2)$$

where *U* is kinetic energy, *V* is voltage, and *v* is particle velocity. Assuming all ions have the same charge, they will have the same kinetic energy, but their velocities will depend on their mass. All ions travel the same distance, so the travel time can be used to calculate their velocity and then mass. Reflectron time-of-flight instruments achieve increased resolution by causing higher-kinetic energy ions to travel further distances to reach the detector.[7,60] Quadrupoles[63] have four parallel rods with opposite pairs of rods

having the same voltage oscillating at a radio frequency rate. Quadrupoles stabilize or destabilize the paths of ions passing through the rods based on their *m/z* ratio. Only ions with a particular *m/z* ratio reach the detector, so a quadrupole can select ions with a particular *m/z* ratio, or the voltage can be continuously varied to scan through ions with a range of *m/z* ratios. In a Fourier transform ion cyclotron resonance mass spectrometer (FTICR-MS),[54,63] ions reside in a Penning trap where they cycle in a fixed magnetic field. An oscillating electric field perpendicular to the magnetic field excites ions to a larger cyclotron radius and causes ions to move in phase with one another. The image current from these ions is measured, with particles of a particular *m/z* ratio producing a sine wave of a particular frequency. This superposition of sine waves from different particles is deconvoluted via a fast Fourier transform (FFT), producing the frequencies and intensities of the different sine waves. Such an instrument produces very high precision results. Because of the mass defect of the elements, such high precision instruments can distinguish between compounds having different chemical formulas but the same nominal mass.

Three dimensional ion traps were invented in 1953 by Paul who won the 1989 Nobel Prize for his work enabling studies of single ions and even single electrons with high precision.[93] Since their invention, ion traps have been developed with many different designs and have played an important role in MS. Ion traps can act as both a storage device and as a mass analyzer. Current tandem ion trap instruments are small, relatively inexpensive, have high sensitivity, and are capable of performing many rounds of MS on a sample.[107] Ion traps have a high mass range and variable mass resolution. They are also able to operate at a higher pressure, usually around 1 mtorr, which does not require

differential pumping. In smaller ion-trap designs, ion trajectories involved in mass analysis are shorter, enabling even higher operating pressures to be used. Collisions of ions with background gases such as helium can also increase the resolution. Recently, cylindrical ion traps (CITs) with simple geometry, have been developed as miniature mass analyzers.[8] Miniaturization of ion traps has also been a focus for magnetic,[50,80,81] time-of-flight,[14,31] quadrupole,[32,71] and even FT-ICR[68] mass spectrometers.

1.4 Detectors

The final component of a mass spectrometer is the detector. Detectors count the number of ions with different mass-to-charge ratios. Electron multipliers are the most common type of detector. They consist of several sets of metal plates at different voltages. When an electron hits the first plate, a process called secondary emission causes roughly one to three electrons to be emitted. These electrons hit the second plate, and even more electrons are emitted. This process continues, until the signal reaches detectable levels. A common type of electron multiplier used in MS is the MicroChannel Plate detector (MCP)[30,53] which amplifies signals from positively charged particles. Position-sensitive MCP detectors have also been developed.[69] Faraday cups[10] and scintillator detectors[30] are also sometimes used.

1.5 Fragmentation Methods in Tandem Mass Spectrometry

Tandem mass spectrometry uses multiple stages of MS with some type of molecular fragmentation between stages.[18,26,54,83] For example, if an initial mass spectrum showed fragments A, B, and C, a second round of MS could select the B fragment and

show the sub-fragments or product ions. Tandem MS instruments can be constructed from multiple physical stages in space or within a single MS stage that traps and stores ions for analysis at a future time.

The most common fragmentation method is collision induced dissociation (CID) or collisionally activated dissociation (CAD)[54,70,83,102] in which the selected ion collides with neutral, inert gas molecules such as helium, argon, or xenon. Many proteins have been analyzed using CID tandem MS, and spectra or "protein sequence tags" of many proteins are available in searchable databases.[70] Another very common method is photodissociation with UV or infrared lasers.[54,83] The infrared multiphoton dissociation (IRMPD) technique is similar to CID in that it involves slow heating of the sample. In the case of proteins, heating with IRMPD may require as much as half a second.[83] Other methods include electron capture dissociation (ECD)[83] where the selected ion absorbs a free electron, and electron transfer dissociation (ETD)[67] where the selected ion absorbs an electron after colliding with a radical anion. Another method is surface induced dissociation (SID) in which the selected ion collides with a surface. The research presented here has focused on SID, since it provides more single-step energy for collision in a much shorter time scale compared to CID. The energy available in CID is given by:[104]

$$E_{COM} = \frac{M_N}{M_{ION} + M_N} E_{LA} \qquad (3)$$

where E_{COM} is the center-of-mass energy, E_{LAB} is the laboratory collision energy, and M_{ION} and M_N are the masses of the projectile ion and neutral respectively. As indicated, the laboratory energy that can be transferred to the internal modes of the projectile ion is limited by the mass of the neutral. Even with a heavy neutral such as xenon, its high

average isotopic mass of 131.30 Da is small compared to a kDa or MDa protein. With SID, if one assumes the mass of the surface is infinite, then $\frac{M_N}{M_{ION}+M_N} \approx 1$ and $E_{COM} \approx E_{LA}$. While the surface mass is not infinite, it is much larger than xenon. CID overcomes this with multiple collisions, though this slow heating of the sample often results in competitive fragmentation pathways and rearrangement products.[29,104] SID also transfers energy much faster, with surface/projectile ion interactions occurring on the order of picoseconds or less.[37,42,54] Activation of large biomolecules such as viruses with SID does not leave as much time for energy to be redistributed throughout the molecule, allowing for more efficient fragmentation compared to CID. In addition, with CID the distribution of energies transferred to projectile ions is much broader than with SID, since CID cannot tightly control the number of collisions. SID also requires no gas load on the instrument and does not require reproducing a specific gas pressure.

1.6 Surface Induced Dissociation

Surface induced dissociation (SID) has been well studied,[1,12,21,24,29,42,54,76,78,104] and a recent review article indicates[37] that analyzed compounds include organic ions, aromatic compounds, organometallic compounds, pseudohalogen ions, fullerenes, clusters, furocoumarins, metalloporphyrines, dendrimers, and doubly charged ions. Studies with SID tandem MS on proteins have also become increasing common.[21,29,104] The use of SID is advantageous over CID for protein analysis because of lower detection limits and easier cleavage of charge-remote sidechains or charged sidechains not immediately near the cleavage site.[37] For example, varying the kinetic energy of the peptide creates observable differences in fragmentation patterns, allowing differentiation of leucine from

isoleucine and glutamine from lysine, thus facilitating peptide sequencing with SID.[21,29,37,54,83,104]

This section will discuss some of the major types of ion/surface interactions and the energy regimes in which these occur. Following this will be a discussion of parameters affecting ion/surface interactions and of different types of surfaces. Finally will be a discussion of why the current research has sought to analyze viruses with SID.

1.6.1 Energy Regimes and Ion/Surface Interactions

Many types of ion/surface interactions are possible depending on the projectile, the surface, their chemical composition and charges, and the kinetic energy of the projectile. This section describes common types of interactions and typical projectile kinetic energies for each type. Four regimes for projectile kinetic energy can be generalized as follows:[37]

1. Thermal range: < 1 eV
2. Hyperthermal range: 1–100 eV
3. Low energy range: 100 eV–100 keV
4. High energy range: 100 keV–100 MeV

The hyperthermal energy regime is of most interest in tandem MS as it contains energies comparable to or greater than typical bond energies. Different types of surface/ion interactions with their respective energy regimes are given in Table 1.[37]

Table 1. Energy regimes of different ion/surface interactions.

Study/Process	**Category(s)**	**General Range**
Elastic Scattering	Thermal	< 1 eV
Physisorption	Thermal	< 1 eV
Dissociative Chemisorption	Thermal, Hyperthermal	< 10 eV
Soft Landing	Thermal, Hyperthermal	< 50 eV
Surface Induced Dissociation	Hyperthermal, Low energy	1 eV – 100 keV
Ion/Surface Reactions (I/SR)	Hyperthermal, Low energy	1 eV – 10 keV
Chemical Sputtering	Hyperthermal, Low energy	1 eV – 10 keV
Ion Implantation	Low energy, High energy	50 keV – 500 keV

With elastic scattering, the projectile bounces off the surface with no change in the projectile or the surface. Closely related to this is quasielastic scattering where the projectile, after bouncing off the surface, has excited vibrational or rotational modes which are not sufficient to produce dissociation. Physisorption or physical adsorption is the adsorption of a molecule to a surface via weak Van der Waals interactions. Chemisorption is the adsorption of a molecule to the surface via interactions stronger than Van der Waals forces. Dissociative chemisorption is the dissociation of molecules after adsorption onto a surface. Typical examples include hydrogen, nitrogen, and oxygen gas. In soft landing, the projectile adsorbs onto the surface intact, in a charged or neutralized state. Surface induced dissociation is an inelastic scattering process in which the projectile bounces off the surface with excited vibrational or rotational states eventually leading to dissociation of the molecule into product ions. Ion/surface reactions (I/SR) involve the exchange of material between the projectile ion and the surface. In chemical sputtering the projectile impact causes charged material from the surface to be ejected. Projectile ion implantation into the surface often accompanies sputtering.

1.6.2 Parameters Affecting Ion/Surface Interactions

The most important factor affecting ion/surface interactions is the choice of the projectile ion and the surface.[37] Their charge, electronegativity, polarizability, shape, and density are among some of the major factors influencing energy and charge transfer efficiencies as well as reaction pathways. Another important factor is the amount of vibrational and electronic coupling of the projectile and surface. For example, in one experiment the change from a self-assembled hydrocarbon surface to the corresponding deuterated surface caused a change favoring vibrational excitation over electronic excitation in scattered fluorocarbon ions.[6] The interaction time of projectile ion/surface collisions is also influential. One study estimated the lower limit of this interaction time on the order of femotoseconds,[42] which is very short compared with the time scale of molecular motion, such as complex chain deformation. This would suggest that only electronic energy can be equilibrated during a collision process and that dissociation of the projectile usually occurs after the collision. Experiments measuring both the velocity and kinetic energy of product ions suggest, however, that this is not always the case. Sometimes product ions have the same kinetic energy,[17,75,78] while at other times they have the same velocity.[16,87,88] When dissociation occurs at the surface, all ions are accelerated away from the surface by the same electric fields, giving them the same kinetic energy. When dissociation occurs after the collision, product ions have the same velocity but different kinetic energies. Another important parameter is the penetration depth of the projectile ion during a collision, which is strongly related to the projectile's kinetic energy and the hardness of the surface. The incidence angle has also been considered in relation to energy transfer efficiency. One molecular dynamics simulation showed[78] that

the internal energy of the excited projectile ion is not strongly dependent on incidence angle, although a slight maximum exists at 45˚. This study also showed that vibrational excitation predominates. The electronic, vibrational, and rotational states of the projectile are also influential. Generally, translational energy is equally as effective at producing dissociation as vibrational excitation.[42] However, in the case of a late barrier where stretching or bending of a particular bond is required to produce dissociation, vibrational excitation is much more effective. Rotational excitation can also be effective if collision orientation is important. The kinetic energies of product ions have been reported up to 15 eV, though most are only a few eV.[37]

1.6.3 Target Surface Composition

The composition of the surface and adsorbates added to the surface can influence the neutralization probability, the sticking probability, the internal energy uptake, and the nature of reactions during the collision.[37] Adsorbates added and their coverage can change the work function, [51] the energy[52] and charge transfer efficiencies,[48] and the density of occupied vibrational states at the surface.[96] When understanding the underlying process of the surface collision is important, crystalline surfaces are often used as these simplify their characterization in theoretical models. Similar studies of metal surfaces requires cleaning the surface. Cleaning metal surfaces must be done in vacuum[37] via high energy argon or oxygen ion beam to remove adsorbates followed by flashing the surface at a temperature above 1000 K. One disadvantage of metal surfaces is their low work function and thus high charge transfer efficiency which can cause neutralization at the surface upon impact. Surfaces or adsorbates should be chosen carefully to avoid neutralization

with SID. Organic adsorbates with high ionization energies meet this requirement, with functionalized hydrocarbon self-assembled monolayers (SAMs) being the most common. A SAMs surface consists of a functionalized hydrocarbon covalently bounded via sulfur to gold or silver. The use of gold or silver changes the tilt angle of the chains and affects the microscopic incidence angle, whereas the length of the chains determines the hardness of the surface and hence the amount of translational energy transferred to internal energy.[43,86] Fluorocarbon SAMs surfaces have seen increasing use.[37] These surfaces resist contamination by water vapor and other components in the air and have high ionization energies of about 14 eV, which minimizes neutralization.

1.6.4 SID Mass Spectrometry of Viruses

This section will begin with a brief description of viruses, followed by a review of previous mass spectrometry studies of whole-virus, and then a discussion of how the present research seeks to extend this work with tandem MS approaches. Viruses are sub-micron sized particles that infect animals, plants, and bacteria. Unable to replicate by themselves, viruses infect a host cell and use the cell's machinery to replicate themselves. A single virus particle, called a virion, is composed of DNA or RNA, enclosed in a protective protein container called a capsid. Viruses come in different shapes including helical (long and narrow), icosahedral (polyhedral or nearly spherical), enveloped (with a phospholipid bilayer), and complex which may have a head and tail. Viruses are classified by the types of life forms they infect.

The life cycle of viruses varies greatly between species although six common stages[22] are cell attachment, penetration, uncoating, replication, assembly, and release

from the cell. In cell attachment, a virus recognizes its host and attaches itself to the host cell's surface. The specificity with which a virus recognizes its host cell determines which types of cells the virus can infect. Virus recognition is specific to ensure that a virus doesn't infect cells in which it cannot replicate itself. Many viruses penetrate the cell using receptor mediated endocytosis or membrane fusion. Once inside, the capsid or protective protein coat is dissolved by viral enzymes or host enzymes thereby releasing the viral DNA or RNA. Other viruses, such as T4, inject their DNA from outside the cell. The cell reads the viral DNA or RNA and produces protein components for making new virions. Assembly is the process by which these protein components join together to make a new virion. Once assembled, viruses leave by killing the cell (lysis) or by budding. Enveloped viruses such as HIV perform budding to obtain a phospholipid bilayer from phospholipids in the cell's wall.

One important characteristic of viruses is the relatively weak bonds that hold together their capsid containers. The bonds between capsid proteins must be strong enough so viruses can survive between host cells, but weak enough so capsids can assemble and disassemble inside the host cell. In the Hepatitis B virus (HBV), the energy of interaction between protein subunits has been measured[20] for the icosahedral T = 4 capsid.[103] For this measurement, *E. coli* expressed HBV capsid protein equilibrated in solution and concentrations of capsids and capsid subunits were measured via size exclusion chromatography. HBV capsids are composed of 120 dimer subunits, and the expression for the reaction is: 120 dimer ↔ capsid. The Gibbs free energy between protein subunits was calculated using the following relationships:

$$K_{capsid} = [\text{capsid}]/[\text{dimer}]^{120} \quad (4)$$

$$K_{capsid} = \prod_j s_i K_{contact} \quad (5)$$

$$\Delta G_{contact} = -RT \ln(K_{contact}) \quad (6)$$

where $\prod_j s_i$ is a statistical term describing the degeneracy of association based on capsid geometry and has a value of $2^{119}/120$. The Gibbs free energy between protein subunits was measured between –2.9 and –4.4 kcal/mol. This Gibbs free energy decreased, and the formation of capsids increased with increasing temperature and salt concentration. Values of ΔG, ΔH, ΔS, and ΔC_p of association were also measured using the method of Baker and Murphy.[9] These results revealed that the enthalpy, ΔH, of this reaction is positive. A negative Gibbs free energy occurs because in the relationship $\Delta G = \Delta H - T\Delta S$ the change in entropy, ΔS, is positive. The positive changes in enthalpy and entropy occur because of the loss of hydrophobic surface during the reaction. Water molecules more readily associate with other water molecules rather than hydrophobic components of capsid proteins. While assembly of capsids from protein subunits causes a local decrease in entropy, burying hydrophobic capsid protein surfaces causes solvating water molecules to be released which increases the overall entropy of the system. Other research suggests that entropy is important in assembly of tobacco mosaic virus,[84] cowpea mosaic virus,[25] and bacteriophage P22.[25] Large patches of hydrophobic surface are common in viral capsid proteins, suggesting that entropy-driving assembly is a common characteristic of viruses.

Whole, intact viruses have been previously studied with electrospray ionization mass spectrometry.[13,27,34,35,58,82,89,92] These studies show that electrospray ionization can vaporize, ionize, and introduce whole viruses into vacuum while maintaining their structure and infectivity. In one study[34] of rice yellow mottle virus (RYMV) and tobacco

mosaic virus (TMV), the authors used an image charge detector to measure the mass and charge states. Since TMV has a mass of 40.5×10^6 daltons and YRMV has a mass of 6.5×10^6 daltons, an image charge detector was necessary to provide a high mass-to-charge (*m/z*) upper limit. Their image charge detector consisted of a small metal cylinder, connected to a charge-sensitive preamplifier, followed by an amplifier. As each positively charged virus particle entered the cylinder, a negative peak was observed in the detector signal. As each particle left the cylinder, a positive peak was observed. The time between peaks was used to calculate the particle velocity. Since the particle was accelerated with electric fields, the particle velocity was proportional to its *m/z* ratio. The amplitude of the peaks was proportional to the particle's charge. This simultaneous measurement of the *m/z* ratio and *z* allowed a rough mass measurement of multiply charged virus particles. The number of charges for TMV and RYMV varied between 300 and 1000 which puts the *m/z* ratio between 40.5×10^3–135×10^3 daltons/charge for TMV and 6.5×10^3 - 21.7×10^3 daltons/charge for YRMV. Both of these are above the 2300 limit of the authors' quadrupole mass spectrometer.

Previous studies have only measured the mass of whole viruses. Many virus capsids, such as Hepatitis B, are held together by weak-protein interactions, suggesting that these capsids could be easily fragmented by surface induced dissociation, yielding observed peaks representative of the masses and numbers of proteins composing the capsid. One well-studied virus is the Coliphage ΦX174.[40] ΦX174 is icosahedral, with a diameter of between 22nm at the depressions and 33 nm at the outermost edges of projections or spikes. The masses and numbers of proteins in this virus are given in Table

2, where the procapsid is formed without DNA inside, and the virion is a mature virus complete with DNA.

Table 2. Protein structural components of ΦX174.

Polymer	Mol.wt (Da)	No. in Virion	No. in Procapsid
Single-stranded DNA	1.73×10^{6}	1	0
B protein	13.8×10^{3}	0	60
D protein	16.9×10^{3}	0	240
F protein	48.4×10^{3}	60	60
G protein	19.0×10^{3}	60	60
H protein	34.4×10^{3}	12	12
J protein	4.2×10^{3}	60	0
Virion	6.43×10^{6}	-	-
Procapsid	9.34×10^{6}	-	-

Our hypothesis is that the SID fragmentation pattern of viruses such as ΦX174 will yield the masses of whole proteins composing the virus. Performing surface fragmentation of viruses provides useful structural information and is a means of studying viruses. In addition, the numbers and masses of different protein types represent a unique signature for each virus and therefore could be used for real-time virus detection. Our research seeks to explore the potential application of SID with viral analysis. Our research also seeks to couple image charge detection with SID, with image charge detection providing an initial mass and charge measurement of whole viruses, SID releasing protonated capsid peptides, and a time-of-flight mass spectrometer analyzing the masses of these peptides. The next chapter will review existing real-time virus detection methods, and the chapter following will describe novel instrumentation coupling image charge detection with SID.

CHAPTER 2

EXISTING REAL-TIME VIRUS DETECTION METHODS

2.1 Introduction

Current methods for real-time virus detection vary in their speed and in the quality of results they produce. According to a recent review,[55] these include traditional and advanced cell culture,[65,72] antigen detection,[38] nucleic acid tests (DNA or RNA), [101] optical methods,[3,38] and microresonators.[39] Important characteristics of a virus detection system are fast processing time, sensitivity, specificity, and repeatability. Sensitivity and specificity depend on the correctness of negative and positive results. Mathematically, these are defined as:

$$\text{sensitivity} = \frac{\text{number of True Positives}}{\text{number of True Positives} + \text{number of False Negatives}} \tag{7}$$

$$\text{specificity} = \frac{\text{number of True Negatives}}{\text{number of True Negatives} + \text{number of False Positives}} \tag{8}$$

Other desirable aspects of a detection system include universality of application to all viruses, low requirements for operator expertise, low cost, and portability. This chapter will begin with a discussion of the most mainstream methods and then move to newer, less-used methods.

2.2 Traditional Cell Culture

Cell culture with traditional tubes[55] is the oldest and most widely used method for virus detection. Typically, the sample is placed in multiple tubes with each containing a monolayer of a particular cell type. The tubes are regularly examined under a standard light microscope at usually 10× power for days or weeks depending on the sample source and the suspected viruses. The effect of a virus on its host cells is called the cytopathic effect (CPE) and is observed as a variation in the cell growth pattern. Generally 2–6 tubes are required for testing each sample, and the CPE for most viruses is observed within 5–10 days.

The influenza virus, parainfluenza virus, and mumps viruses do not have CPE's that are visible under the light microscope. These viruses, however, cause the production of hemagglutinating proteins on the walls of their host cells. Such an infected cell readily adheres to red blood cells, which is easily observable. Such a test of potentially infected cells' affinity for red blood cells is called a hemadsorption (HAD) test and is routinely performed with results appearing in about twelve hours.

Though results from cell culture come slowly (5–10 days), they are very accurate and are considered to be the gold standard. Cell culture methods also distinguish between viable and non-viable viruses, since non-viable viruses will not infect cells. Cell culture readily detects mutant virus strains, detects multiple virus types at the same time, and produces isolates for future analyses.

Cell culture requires technical expertise in recognizing CPE's in cells and in purchasing and maintaining a variety of cell culture types. Generally the costs of performing cell culture tests are low.

2.3 Antigen Detection

Antigens are molecules derived from viruses, bacteria, and other pathogens that stimulate an immune response. Specifically, antibodies bind with antigens and tag them for attack by an organism's immune system. Viral antigens can be detected inside and outside the cell with immunofluorescence (IF) techniques[55] which take 20–30 minutes. IF techniques use fluorescein isothiocyanate (FITC)-labeled monoclonal antibodies (MAbs), and the binding of MAbs to viral proteins produces fluorescence. IF techniques are very specific and sensitive, though they are generally less sensitive than are cell cultures. Exception cases include respiratory syncytial virus (RSV) and varicella-zoster virus (VZV), in which IF is more sensitive than cell cultures, and adenovirus, in which IF is much less sensitive. IF can not be used with some viruses, including polioviruses, coxsackieviruses, and echoviruses in the "enterovirus" group. IF testing is considered to be a demanding technique, and it is available only at advanced laboratories and rarely at community hospitals. The success of IF depends on the virus being detected, specimen type, age of the patient, time of sample collection after appearance of symptoms, MAb reagents, and level of expertise of laboratory personnel. The main limitations of IF include poor sensitivity for some viruses (adenovirus), poor availability of reagents for some viruses, and the inability of IF to differentiate between viable and non-viable viruses.

Non-IF methods for detecting viral antigens include membrane-based enzyme immunoassay (EIAs) in cassette format,[55] optical immunoassays (OIAs),[38,55] and immunochromatographic/lateral-flow (ICLF) systems.[55] EIA and OIA methods use enzyme-bound antibodies that produce a color change in the presence of viral antigens. In

immunochromatographic/lateral-flow (ICLF) systems, the sample mixes with a colored reagent and flows along a solid substrate using capillary action. The substrate has lines or zones, some of which have been treated with antibodies. Depending on the presence or absence of the antigen, the colored sample mixture can become bound to the test lines or zones. The advantages of Non-IF methods are that they are easy to perform and are very fast. The disadvantages are that Non-IF methods have poor sensitivity compared to cell culture methods, they are unable to distinguish between viable and non-viable viruses, and they are only available for respiratory syncytial virus (RSV) and influenza A and B viruses.

2.4 Advanced Cell Culture with Antigen Detection

Shell vials are compact and designed to be placed in a centrifuge to speed viral replication and the appearance of the cytopathic effect (CPE).[55] For example, in cells infected with herpes simplex virus (HSV), the CPE appeared 2.4 times faster when centrifuged at 2 rpm and 6.8 times faster when centrifuged at 96 rmp.[65] Early pre-CPE virus detection is also accomplished with IF antigen detection techniques. Using shell vials increases the possibility of cross contamination; therefore, laboratory procedures must be established to avoid this during sample inoculation, centrifugation, and monitoring. With centrifugation, results from most viruses are available within 24–48 hours.

The disadvantage of centrifugation is decreased sensitivity compared to traditional cell culture. One study reported[72] that for detection of severe cytomegalovirus

(CMV) in blood samples, both traditional cell culture and centrifuged shell vial tests are necessary, since one often detects the virus when the other one doesn't and vice versa.

Cocultivated cells[55] incorporate the growth of multiple cell types in the same vial, for simultaneous detection of multiple viruses. Again, early pre-CPE virus detection is accomplished with IF antigen detection techniques. The advantages of cocultivated cells are the need to maintain fewer cell types and detection of a wider range of viruses.

Another advanced technique is the use of transgenic cells which are genetically modified.[55] These are designed to produce an easily measurable enzyme when a specific virus enters the cell. Although growth times are the same, the advantage is simplified identification of specific viruses. Transgenic cells have been created for HIV-1 and Herpes Simplex Virus (HSV)-2 but are not available for other viruses.

2.5 Nucleic Acid Amplification Tests

Nucleic acid amplification tests amplify viral DNA or RNA via polymerase chain reaction (PCR).[101] First, PCR uses high temperatures (94-98°C) to denature or separate double-stranded DNA into two single-stranded DNA strands. Next the temperature is lowered to 50-65°C and DNA primers anneal or hybridize with their complementary DNA target. Two primers are used, one binding to one DNA strand and the other binding to the complementary DNA strand. Third, a DNA polymerase such as Taq polymerase is used to elongate the sequence of DNA downstream from the primer by adding complementary deoxynucleotide triphosphates (dNTPs). PCR is generally performed for 20 to 35 cycles and produces millions of copies of the target DNA strand. For RNA amplification, the RNA must be copied to DNA using reverse transcriptase. Real-time

PCR can be performed in 2 hours and is very sensitive and specific. It is also useful for viruses that can not be cultured. Three disadvantages of PCR are that it requires technical expertise, is expensive, and will miss mutated viruses.

2.6 Other Methods

Other virus detection methods include optical methods and microresonators. Optical immunoassay (OIA)[38,55] is an antigen detection technique that relies on differences in reflectivity of virus particles compared to virus particles bound to an antibody. Other optical techniques[3] use lasers to detect viral particles in the air using the number, size, and shape of particles. The main disadvantage of this technique is lack of specificity. Microresonators are micromechanical devices with small springs. The resonant frequency changes due to addition of virus particles. The resultant mass measurement provides means for virus identification. The disadvantage of this technique is low specificity.

CHAPTER 3

NOVEL INSTRUMENTATION USING IMAGE CHARGE DETECTION AND SURFACE INDUCED DISSOCIATION FOR VIRUS DETECTION

3.1 Introduction

The novel instrumentation presented here couples image charge detection with surface induced dissociation (SID) as given in Figure 1. The instrument used electrospray ionization, a technique capable of producing charged, intact viruses. After ionization, sample particles entered the vacuum through an aerodynamic lens which focused them into a narrow beam and accelerated them to 100–300 m/s. After the aerodynamic lens, the ionized samples passed through two skimmers necessary for achieving high vacuum. Next, they were accelerated with pulsing electric fields of up to 10 kV. Following this, mass and charge measurements were made using image charge detection, followed by collision with a surface and analysis of the released capsid peptides using a reflectron time-of-flight mass spectrometer with a microchannel plate (MCP) detector.

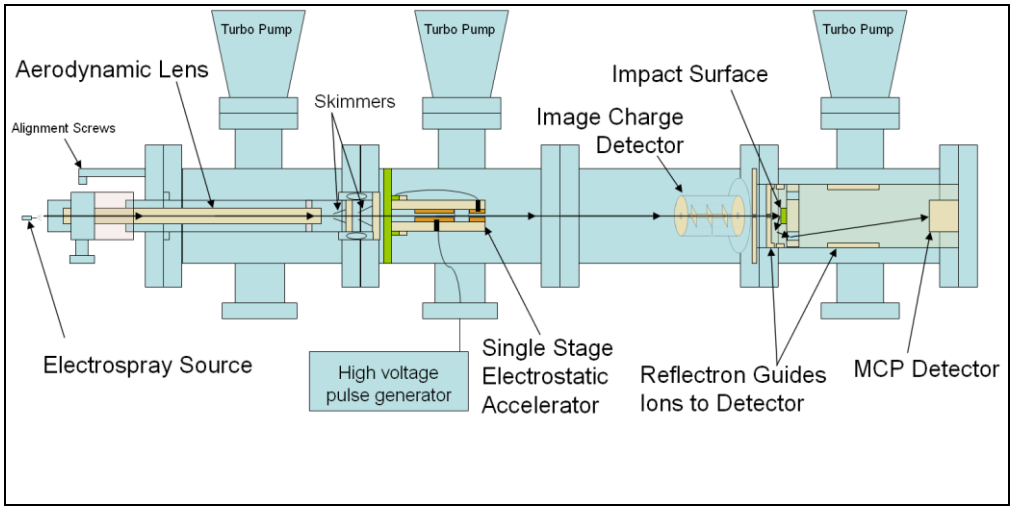

Figure 2. Image charge detection, surface induced dissociation mass spectrometer.

This chapter will describe improvements on each component of the system, including design decisions, alternative approaches tried, and the resultant performance observed.

3.2 Electrospray Ionization Source

Electrospray ionization[23,28,41,44,45,47,66,85] is a robust, soft-ionization technique and was chosen because of its ability to create intact, air-born virus particles from liquid samples.[13,27,34,35,58,82,89,92] This research sought to achieve complete desolvation, and began by using smaller samples, since these have a lower mass-to-charge ratio. For samples that are spherical and have a fixed number of charges per unit surface area, the mass-to-charge ratio decreases with decreasing radius, since surface area decreases more slowly than volume as radius decreases. Since our accelerator uses electric fields to accelerate electrosprayed sample particles, having less mass and more charge allows higher velocities to be achieved. More specifically, the properties of electrospray droplets are given by the following equations:[23,36]

$$R = \left(\frac{3\varepsilon\gamma^{1/2} V_f}{4\pi\varepsilon_0^{1/2} KE} \right)^{2/7} \tag{9}$$

$$q = 0.5[8(\varepsilon_0\gamma R^3)^{1/2}] \tag{10}$$

$$E = \frac{2V_c}{r_c \ln(4d / r_c)} \tag{11}$$

where R is droplet radius, q is droplet charge, E is the applied electric field at the capillary tip, γ is the surface tension of the solvent, ε is the permittivity of the solvent, ε_0 is the permittivity of vacuum, V_f is the flow rate of the solution, K is the conductivity of the solution, V_c is the applied voltage, r_c is the capillary outer radius, and d is the

distance from the capillary tip to the counter-electrode. While the above equations are based on unproven assumptions about the electrospray mechanism,[62] they nevertheless give predictions of the right order of magnitude and provide information for achieving small electrospray droplets. For this research, achieving complete desolvation required low flow rate (V_f), a high voltage (V_c), and a small capillary outer radius (r_c).

Many different types and sizes of electrospray capillaries were employed for this research. These were composed of stainless steel, fused silica, and a nickel-cobalt alloy. The stainless steel capillaries were prepared from tubing with inner diameters (i.d.) ranging from 38.1 to 63.5 μm. These were prepared by fastening the tubing in larger 1/16 inch outer diameter (o.d.) tubing with epoxy. The tips were then manually sharpened with a drill press and sand paper. Later, fused silica capillaries were obtained from Polymicro (Phoenix, AZ). These were also secured into the same 1/16 inch o.d. tubing with epoxy. The capillary tips were then sharpened according to a procedure in the literature[46] involving chemical etching with hydrofluoric acid (HF). As the fused silica tips were dipped in the HF, water was pumped through the inside of the capillary. This allowed the HF to eat the outside of the immersed section of capillary, while the flow of water protected the inner part of the capillary from the acid. The result of this procedure was atomically-sharp capillary tips with inner diameters of 20, 10, and 5 μm. One disadvantage of the fused silica capillaries is their poor electrical conductivity compared to stainless steel. For this reason, it was advantageous to have fused silica capillaries protruding shorter distances from the larger 1/16 inch o.d. stainless steel tubing in which they were housed. The use of concentrated HF also required special equipment and training to ensure proper safety. Nickel-cobalt tubing was obtained from Valco

Instruments Inc. (Houston, TX) and had an i.d. of 25.4 μm and an o.d. of 360 μm. These tips were manually sharpened in the same manner as the stainless steel capillaries. The large o.d. made this tubing rigid and thus easier to work with than the stainless steel or fused silica. Also, the nickel-cobalt alloy is electrically conductive. In addition, Valco Instruments later sent us custom-made tubing with reduced i.d. of 5 μm and 2 μm, as well as machine-sharpened 25.4 μm i.d. tubing. Of the stainless steel, fused silica, and nickel-cobalt electrospray capillaries, the stainless steel tubing experienced the least problems with clogging. The most commonly used size was the 63.5 μm i.d. capillary which never clogged. The fused silica capillaries were very sharp, though clogging was quite problematic. The nickel-cobalt capillaries had problems with clogging as well, though these were easier to make and clogging occurred less-frequently than the fused silica, especially with the 25.4 μm i.d. size.

Two additional techniques for achieving complete desolvation used heated gas. The first involved connecting a heated stainless-steel capillary to the inlet of the vacuum system, so that electrosprayed particles entering vacuum would have to pass through this and be desolvated by the heated air inside. The capillary was 10 cm long with an i.d. of 0.01 inch or 254 μm. It was heated by passing a current through heating wire wrapped around the outside, until the temperature was in the range of 100–175 ˚C. To ensure proper vacuum, a small Viton o-ring formed a three-way seal between the heated capillary and two metal plates as depicted in Figure 3.

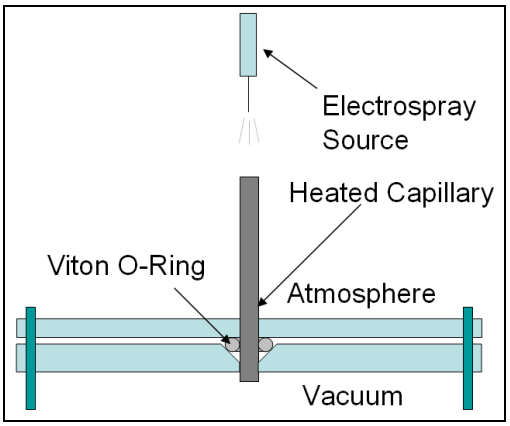

Figure 3. Heated desolvation capillary.

The second method used for desolvation involved the use of heated nitrogen (N_2) gas near the electrospray source. The gas flowed around the electrospray capillary, with faster flow near the tip as depicted in Figure 4.

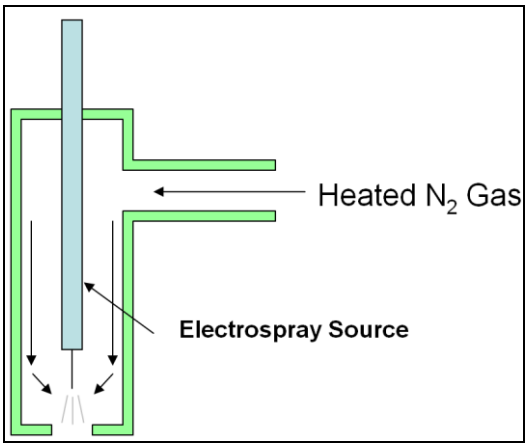

Figure 4. Desolvation with N_2 gas.

The material enclosing the gas near the capillary tip was made of non-conducting Teflon to ensure the spray was only attracted toward the vacuum inlet. The temperature of the gas was 100–175 ˚C. The flow rate of the gas was measured using a bubble meter with the electrospray turned off.

The last electrospray setup made was a filling needle with heated N_2 desolvating gas. With this setup, the electrospray fluid was pumped through 20 µm i.d. fused silica tubing inserted into a large, 22 gauge (0.0253 inch i.d.) stainless steel filling needle through which the heated N_2 gas flowed. The fused silica extended almost to the end of this stainless steel needle. The large droplets produced by the voltage applied to the stainless steel needle were desolvated with the N_2 gas as depicted in Figure 5.

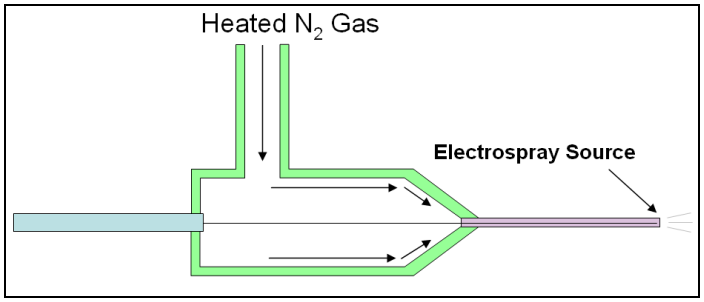

Figure 5. Filling needle electrospray source.

Commercial instruments are built with specially manufactured tips similar to this filling needle, and desolvation is enhanced by the small i.d. of the needle through which the gas flows. Such instruments also obtain better desolvation by placing the electrospray source slightly off-axis with the vacuum inlet. Filling needle type setups like this one have the advantage that they produce very good desolvation and do not require sharpening of the capillary tip. They also can have higher fluid flow rates and require a lower N_2 gas load compared to the setup in Figure 4 because of the smaller i.d. needle. Replacing clogged fused silica tubing in the filling needle is also very simple. Both the filling needle setup and a small i.d. sharpened electrospray tip with a heated capillary are sufficient to achieve complete desolvation.

This experiment was designed to accommodate electrospray solutions composed of biological and non-biological samples. One non-biological sample contained 240 nm diameter amino-polystyrene microspheres prepared according to procedures in a previous study of 910 nm diameter amino-polystyrene microspheres.[19] These 910 nm particles were prepared in a 4:1 methanol:water mixture with a pH reduced to 3.9 using acetic acid. The concentration of the particles was 0.05% (w/v) or 1.2×10^{9} particles/ml. Using this low concentration ensured there was, at most, one sphere per electrospray droplet, though the authors state that concentrations an order of magnitude higher are also sufficient. The results from electrospray mass spectrometry of the 910 nm spheres demonstrated numbers of elementary charges in the range of 10^{2} to 10^{3}, producing surface charge densities between 3.8×10^{-6} and 3.8×10^{-7} elementary charges per square angstrom. With charges per surface area in this range, the number of elementary charges on 240 nm diameter amino-polystyrene spheres lies between 7 and 70. With the given density of 1.05 g/cm^{3}, their mass to charge ratios lie between 6.6×10^{7} and 6.6×10^{8} daltons per elementary charge. This reported charge per surface area ratio is unusually low, considering that the maximum charge per surface area predicted by the Coulomb repulsion model is about three orders of magnitude higher.[45]

Electrospraying viruses required obtaining virus samples as well as determining the appropriate solvent to use. Virus capsids will dissolve in concentrated methanol solutions with low pH, so finding a less corrosive solvent and appropriate pH levels was necessary. In one study of MS2 virus,[92] the viruses were electrosprayed from neutral pH water in the absence of buffer from a specially-prepared gold-plated borosilicate needle with a nanoflow rate and a virus concentration of 5 μM or 3×10^{15} particles/ml. This

concentration was the highest observed in the literature. In a study of tobacco mosaic virus (TMV) and rice yellow mottle virus (RYMV),[82] the samples were desalted by centrifugal filtration and resuspended in distilled water. In a study of Cricket Paralysis Virus (CrPV),[27] the virus particles eluted through a chromatographic column and were then immediately electrosprayed. Depending on the time of elution, the solvent was some combination of water and acetonitrile, with 0.1% trifluoroacetic acid (TFA). One study[104] employing SID states that electrospraying biological samples is best done in water at neutral pH. It was recognized that use of a water solvent would not work with the filling needle electrospray setup, but the stainless steel, fused silica, or nickel-cobalt capillaries with a nanoflow rate and heated capillary were deemed sufficient.

Virus samples of coliphages ΦX174 and T4 were obtained from Carolina Biological in Burlington, NC. As stated, ΦX174 is icosahedral with a diameter between 22–33 nm and a mass of 6.43 MDa. The T4 virus has a head that is prolate in shape with a diameter between 78 and 111 nm, and a mass of about 320 MDa. T4 also has a tail with a length of 113 nm and a width of 16 nm. The reported concentration of ΦX174 virus sample was 9×10^{9} particles/ml. Examination of the ΦX174 sample under an electron microscope showed no visible capsids, after which procedures were undertaken to replicate and concentrate the virus. A kit was ordered from Carolina Biological with materials for replicating both ΦX174 and T4 in their *E. coli* hosts. Growing *E. coli* required multiple attempts, as did replicating the viruses. After replication, purification of the product was required. Information for purification of the ΦX174 products was found, though purification was not completed. Other virus samples were found, however, including a Hepatitis B procapsid, and a satellite tobacco mosaic virus.

3.3 Image Charge Detection

The image charge detector was used to obtain the first mass-to-charge measurements in this tandem mass spectrometer and was one of the first components to be successfully tested. The charge sensitive preamplifier was an Amptek (Bedford, MA) A250 on a PC 250 circuit board, and the amplifier was an Ametek/Signal Recovery (Oak Ridge, TN) 5113 model. As indicated in Figure 6, the first charge detector design consisted of three cylinders parallel to the particle beam axis, each having a 38.1 mm length and a 5.35 mm i.d. The center cylinder was connected to the preamplifier, and shielding was provided by the outside stainless steel casing as well as the two outside cylinders.

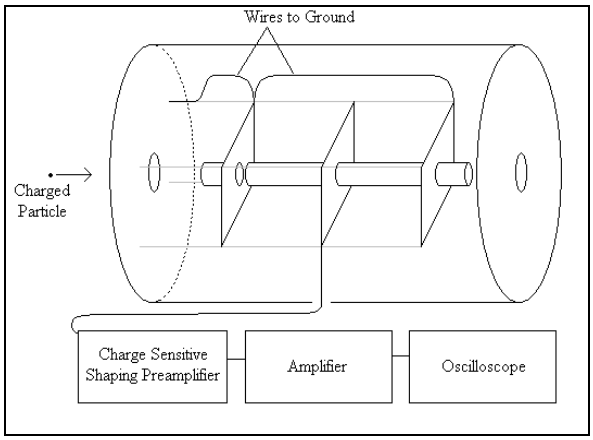

Figure 6. Image charge detection instrumentation.

Initial testing of the A250 and amplifier was done with a low voltage pulse generator and a voltage divider connected to the A250. With the oscilloscope trigger using the pulse generator signal, the amplified A250 signal was observed to have the same frequency with averaging at only 10 sweeps. While testing in vacuum, it was first

determined that electrosprayed particles were reaching the detection region by using a Faraday detector and a picoammeter. The charge detector was then used to detect the electrosprayed particles with the A250 and amplifier. An example signal is given in Figure 7.

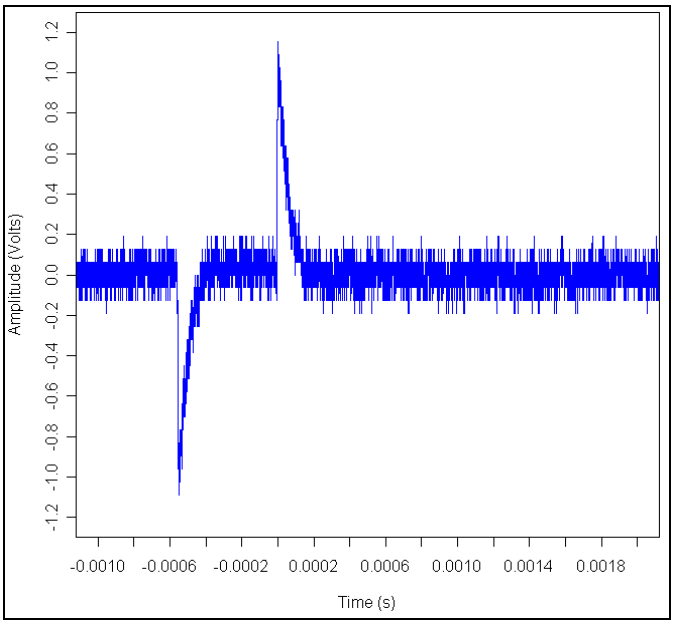

Figure 7. Image charge detector signal from a positively charged electrospray particle.

The time between the negative and positive peaks approximates the time required for the particle to pass through the detection cylinder and can be used to calculate particle speed. The amplitude of the positive and negative peaks is proportional the charge on the particle. More specifically, the A250 preamplifier[2] produces a voltage:

$$V_0 = \frac{Q_D}{C_f} \tag{12}$$

having a decay time constant:

$$\tau_f = \frac{R_f}{C_f} \tag{13}$$

where Q_D is the total charge seen during the pulse, C_f is a feedback capacitor, and R_f is a feedback resistor. Achieving large V_0 and τ_f values requires having C_f as small as possible and R_f as large as possible. Values used for these were 1 pF and 1 GΩ, respectively. Later, C_f was lowered to 0.1 pF. The number of charges on a particle can be calculated by rearranging equation 12 as follows:

$$Q_D = V_0 C_f = \frac{V_s}{V_g} \times C_f \tag{14}$$

where V_s is the voltage on the oscilloscope and V_g is the gain on the amplifier. This calculation assumes the current seen equals the charge on the particle. A better approach would be to calibrate the charge detector by measuring the charge on a particle carrying a known number of charges and then scale other measurements by the same constant. Calibration was also discussed in one study,[33] though they do not appear have used an A250. For a particle accelerated through a known voltage, the mass can be calculated by rearranging equation 2 from section 1.3 as follows:

$$m = \frac{2Q_D V}{v^2} \tag{15}$$

where V is the known voltage and v is velocity due to acceleration through the voltage. For this experiment, acceleration from the aerodynamic lens also had to be accounted for (see appendix).

Significant electrical noise was encountered when the charge detector was used in vacuum with the electrostatic accelerator and the turbo pumps used to reaching the high vacuum required by the MCP detector. The turbo pumps spin at 860 rps, and the frequency of the observed noise was 860 Hz. Setting the frequency filter on the Ametek amplifier to allow only 30–300 kHz signals reduced the noise but did not remove it

entirely. The accelerator pulses at 10 kV every 0.00127 s, producing very short, mainly downward spikes in the charge detector signal. An example of the noise is given in Figure 8. In this signal, much of the accelerator noise has been removed by wrapping the charge detector and other wires with aluminum foil, though some downward spikes are still present.

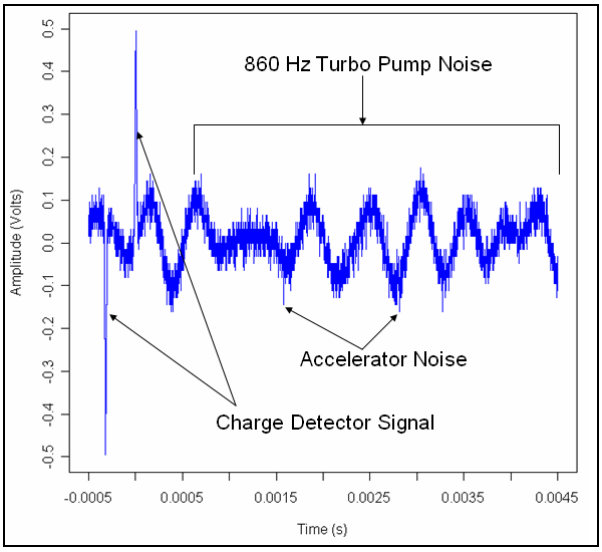

Figure 8. Image charge detector signal with turbo pump and accelerator noise.

Setting the oscilloscope trigger slightly above the turbo pump noise allowed particles to be observed. Special software was also written to automatically process charge detector signals and produce particle velocities and amplitudes. This software removed the accelerator spikes with a median filter before looking for maxima and minima.

Much time was spent trying to achieve higher particle speeds, which involved detection of smaller particles with lower mass-to-charge ratios. This was difficult, first because it required setting the oscilloscope trigger below the level of the turbo pump noise. Second, the error in the Amptek A250 is 100 electrons RMS. The 240 nm amino-polystyrene spheres that were often used had numbers of elementary charges between 7

and 70 making them difficult to detect. The spheres also had high mass-to-charge ratios making them difficult to accelerate.

At first, only the charge detector resided in vacuum, and the A250 and amplifier were outside vacuum. Later, the A250 was placed in vacuum very close to the charge detector. This did not reduce the noise significantly. It was then discovered that cell phones generate signals in the charge detector with the same shape as those produced by electrosprayed particles. The distance between positive and negative peaks is always the same with cell phone signals. This discovery led to the realization that radio frequency interference (RFI) or electromagnetic interference (EMI) was causing noise in the charge detector signal. While any sufficiently conductive material such as stainless steel will block static electric fields, stopping static magnetic fields cannot be done with a simple conductive material, although magnetic flux lines can be redirected by introducing eddy currents using a high permeability or magnetic material.[74] When blocking electromagnetic waves, the skin depth, or the distance for an electromagnetic wave to be attenuated 1/*e* or 37%, depends on the frequency of the wave and the material:[94]

$$\delta = \frac{1}{\pi f \mu \sigma} \tag{16}$$

where f is frequency in MHz, μ is relative permeability, and σ is conductivity relative to copper in the International Annealed Copper Standard (IACS). Skin depth increases and absorbance decreases at lower frequencies with lower permeability and conductivity materials. Therefore, materials like copper, aluminum, or mild steel are better than stainless steel for absorbing lower frequency electromagnetic waves. For this reason, the stainless steel casing enclosing the charge detector was replaced with copper. In addition, the Ametek 5113 amplifier was replaced with an Amptek 275 amplifier, with three of

these units residing on a PC275 circuit board. The new copper casing allowed the charge detector, the A250 pre-amplifier, and the A275 amplifier to all reside in vacuum very near one another. Wrapping all wires in aluminum foil, including those connecting the accelerator and the microchannel plate (MCP) detector also reduced noise. Wrapping MCP wires with foil also reduced accelerator noise in the MCP detector to acceptable levels. Turbo pump noise was not observed in the MCP detector. In addition, a thin sheet of copper was placed in-vacuum after the accelerator to help contain noise near the source.

3.4 Aerodynamic Lens

The aerodynamic lens in this instrument served to focus electrosprayed particles into a narrow beam and improve the efficiency with which they passed through the sub-millimeter sized skimmers. Aerodynamic lenses,[56,57,97,98,99,100,105,106] depicted in Figure 9, consist of a number of spacer chambers separated by lenses each with a small millimeter-size orifice in the center.

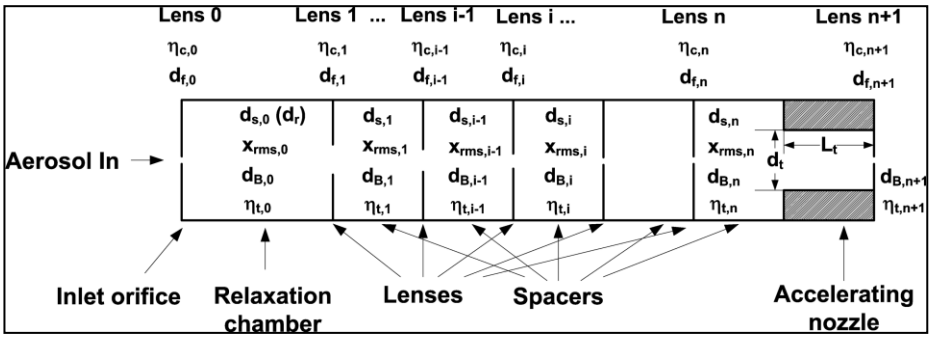

Figure 9. Aerodynamic lens schematic. "Aerosol Science & Technology: A Design Tool for Aerodynamic Lens Systems. *Aerosol Sci. Technol.*"(40): 320–334. Copyright 2006. Mount Laurel, NJ. Reprinted with permission.[99]

The region before the aerosol inlet was at atmospheric pressure, and the pressure after the last spacer was in the millitorr range, with each lens serving to lower the pressure and focus particles. Inside the last chamber was an accelerating nozzle. Its purpose was to set the operating pressure, accelerate the particles, and minimize particle divergence angles.[99]

Wang and McMurry developed lens calculator software to assist in the design of aerodynamic lenses.[99,100] This lens calculator used three measures of performance: beam diameter, transmission efficiency, and particle flow terminal velocity. Beam diameter is defined as the diameter enclosing 90% of the particles. Transmission efficiency is the percentage of particles retained in the beam. Particle terminal velocities are the final velocities of particles after passing through all lens elements. Adjustable parameters in the lens calculator include the starting and ending pressures, flow rate, particle density and diameter, orifice diameters, and spacer diameters and distances. The input parameters used to obtain lens dimensions for this instrument are given in the appendix.

3.4.1 Beam Contraction in Aerodynamic Lenses

An aerodynamic lens element reduces the particle beam width as particles pass through the orifice. As described by Lui, et. al.,[56] the radial location of a particle can be described as a function of the distance *d* after the orifice or $r_p(d)$. As a particle approaches the lens orifice, it follows a streamline at radial location $r_0(-\infty)$. After passing through the lens, the particle radial location $r_p(\infty)$ diverges from the streamline radial location $r_0(\infty)$ as indicated in Figure 10.

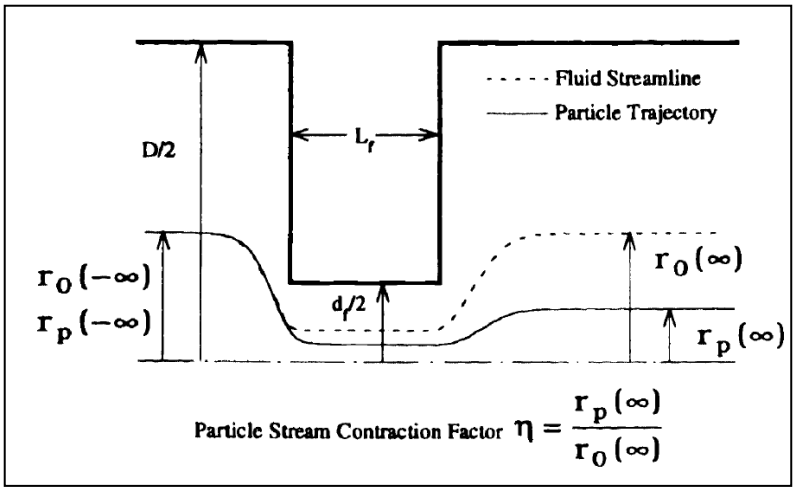

Figure 10. Beam contraction in an aerodynamic lens element. "Aerosol Science & Technology: Generating Particle Beams of Controlled Dimensions and Divergence: I. Theory of Particle Motion in Aerodynamic Lenses and Nozzle Expansions. *Aerosol Sci. Technol.*"(22): 293–313. Copyright 1995. Mount Laurel, NJ. Reprinted with permission.[56]

One way of measuring the difference in beam width before and after an orifice is the particle stream contraction factor η defined as:

$$\eta = \frac{r_p(\infty)}{r_0(\infty)} \tag{17}$$

An aerodynamic lens functions optimally when the particle stream contraction factor η approaches zero. The particle contraction factor η is a strong function of the Stokes number (*St*):

$$St = \frac{V_0 \tau}{d_f} \tag{18}$$

where V_0 is the initial particle velocity, τ is the relaxation time or the time for a particle to reach 1/*e* of its terminal velocity, and d_f is the orifice diameter. The quantity ($V_0 \tau$) is called the stopping distance of the particle. The particle contraction factor η relates to the Stokes number (*St*) as follows:

$|\eta| \approx 1$ when $St << 1$,

$|\eta| < 1$ when $St \approx 1$

$|\eta| > 1$ when $St >> 1$.

There is an optimal stokes number (St_0) for which $\eta = 0$. The optimal Stokes number is a function of the flow Reynolds number, Mach number, and lens geometry.[56,99,105]

3.4.2 Aerodynamic Lens Calculator Assumptions

The lens calculator assumes that particles are spherical and electrically neutral. Though particles in this application were charged, the concentrations of particles were not deemed high enough to be a cause for concern. The lens calculator also assumes that the flow is well-behaved, or that it is subsonic, continuum, and laminar. Subsonic conditions occur when the Mach number is less than one:

$$Ma = \frac{u}{c} < Ma^* \approx 1 \tag{19}$$

where u is the flow velocity, and c is the speed of sound in the medium, and Ma^* is the Mach number of choked flow[97] and is close to one.

Laminar flow, the opposite of turbulent flow, occurs when a fluid flows in parallel layers with no disruption between the layers. More specifically, laminar flow occurs at low Reynolds numbers. The authors of the lens calculator use a Reynolds number of 200 as the cut off, so that laminar flow occurs according to the condition:

$$\mathrm{Re} = \frac{4\dot{m}}{\mu\pi d_f} < 200 \tag{20}$$

where $\dot{m}$ is the mass flow rate, μ is the carrier gas viscosity, and d_f is the orifice diameter.

Continuum flow occurs with low Knudsen numbers, and the authors of the lens calculator use 0.1 as the cut-off value. Therefore,

$$Kn = \frac{2\lambda}{d_f} < 0.1 \tag{20}$$

where λ is the mean free path of the gas molecules upstream of the orifice, and d_f is the orifice diameter.

3.4.3 Brownian and Lift-Force Broadening

Two effects contributing to beam broadening are Brownian and lift-force broadening.[56] Brownian broadening is the freezing of random, radial particle motion as particles pass through a lens orifice. At higher pressures, the gas particle collision rate is high. Though particles collide, they may be considered to follow a generally straight path. As the pressure drops, however, collisions become significantly less frequent. Whatever radial motion a particle had before the orifice becomes frozen after it passes through the orifice into a lower pressure chamber. This freezing of particle radial motion creates Brownian broadening as illustrated in Figure 11. The distribution of radial particle speeds approximates the Boltzmann distribution.

Lift forces also contribute to broadening in beams composed of non-spherical particles. Lift forces are the sum of the fluid dynamic forces acting on a body that are perpendicular to the direction of the external flow relative to the body. An example of lift is seen in the wing of an airplane. As air moves horizontally over a wing's surface, the shape of the wing creates a higher pressure below the wing compared to above the wing, thereby creating lift.

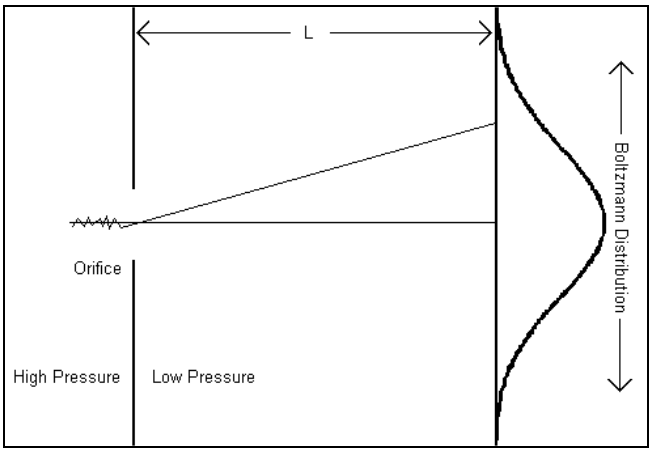

Figure 11. Brownian broadening due to random radial motion. "Aerosol Science & Technology: Generating Particle Beams of Controlled Dimensions and Divergence: I. Theory of Particle Motion in Aerodynamic Lenses and Nozzle Expansions. *Aerosol Sci. Technol.*"(22): 293–313. Copyright 1995. Mount Laurel, NJ. Reprinted with permission.[56]

Mathematical models[56] demonstrate how lift forces affect objects of differing shapes including cylinders, discs, spheroids, and cuboids. For simplicity, these models do not consider object rotation, but assume objects are positioned at a given angle with respect to fluid flow. These studies show that lift force broadening generally is greater than Brownian broadening. This suggests that particle beam widths will be greater for irregularly shaped particles such as the long, helical tobacco mosaic virus.

3.5 Electrostatic Particle Accelerator

The electrostatic particle accelerator, depicted in Figure 12, consists of two cylinders with the first pulsing between ground and high voltage. The maximum allowed voltage on the pulse generator was 10 kV.

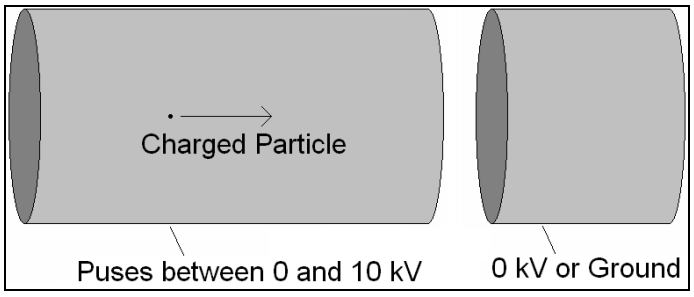

Figure 12. Electrostatic particle accelerator.

Ideally, charged particles enter the first cylinder when it is uncharged, and the cylinder becomes charged while the particle is inside. In this case, the charged particle does not experience an electric field because it is in the center of the cylinder. As, the particle leaves the cylinder, it experiences an electric field and is accelerated toward the second cylinder which is at ground. No more than half the particles can be accelerated, since some particles try to enter the cylinder when it is charged. The timing of the accelerator must be adjusted to match the average velocity of the incoming particles.

Simulations were done modeling how particles passed through the accelerator using SIMION 7 software.[64] These results showed that particles were required to be in the very center of the accelerator in order to reach the detector. Alignment of the aerodynamic lens with the two skimmers and accelerator was therefore deemed crucial. The alignment was checked by removing the mass spectrometer, shining an LED light through the system, and observing the light on the other side. Alignment of the end of the aerodynamic lens closest to the first skimmer was achieved via tight fit and well machined components. Alignment of the other end was achieved via the alignment screws on the front of the instrument which changed the direction the aerodynamic lens pointed. The second skimmer was more difficult to align with the first skimmer, since it resided on a disk separating two vacuum chambers. After manual adjustment, the LED

light was observed passing through these components without significant deviation vertically or horizontally. The accelerator and second skimmer were attached to same plate, and accelerator alignment with the second skimmer was achieved via tight fit and precise machining.

In addition to checking the alignment with the LED light, a Faraday detector was built to check the alignment. This detector had a circular center plate and three side plates as depicted in Figure 13.

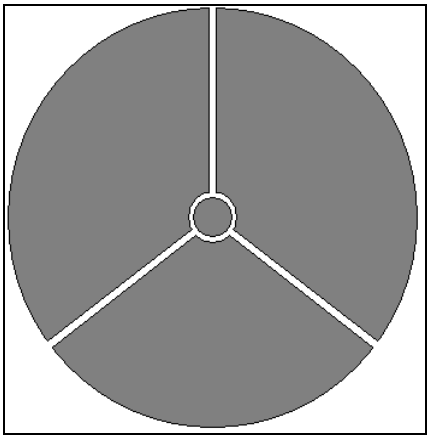

Figure 13. Faraday detector used for alignment.

These four plates were separated from one another by thin metal walls over an inch high to prevent particles from colliding with multiple plates. This Faraday detector was placed in vacuum temporarily to check alignment. The Amptek A250 preamplifier and the Ametek 5113 amplifier were attached to each of these plates, and individual particles were counted. Observing on which plate more particles impacted allowed the alignment to be fine-tuned. After this process, particles were still observed impacting on all three plates, though a greater number of particles was observed on the center plate.

As a result of the wide particle spread observed with the Faraday detector, wire mesh grids having 45 wires per inch were placed on the end of the accelerator cylinder and the start of the ground cylinder. Figure 14 shows SIMION[64] simulations with grids being absent or present on the two cylinders.

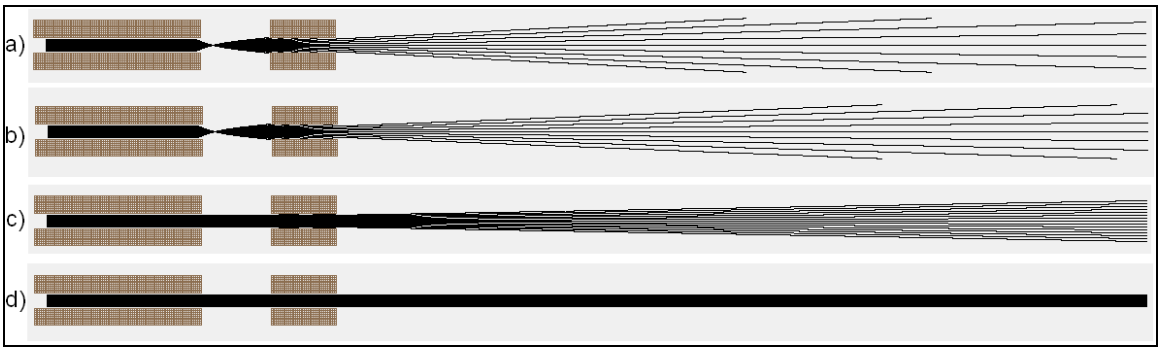

Figure 14. SIMION simulation of particles passing through the accelerator at different radial distances. Simulation (a) was without grids; (b) was with one grid on the ground cylinder; (c) was with a grid on the high voltage cylinder; (d) had grids on both cylinders.

As indicated, having grids on both the high voltage and ground cylinders circumvented the requirement for particles to be in the center of the accelerator, though passage through each grid caused particle losses of about 10%.

3.6 Mass Spectrometer

Two different time-of-flight (TOF) mass spectrometer setups were used in this experiment. The first was a reflectron consisting of an impact plate and several cylinders. A cross section of the reflectron is depicted in Figure 15.[7]

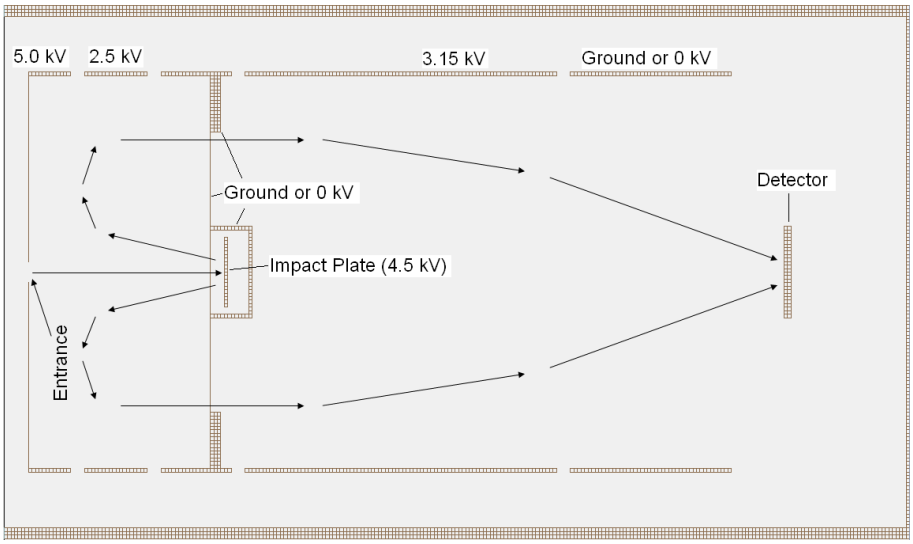

Figure 15. Reflectron mass spectrometer cross section.

The detector used was a microchannel plate (MCP) 25mm z-gap detector from R. M. Jordan (Grass Valley, CA). A VT120 Fast Timing Preamplifier from Ortec (Oak Ridge, TN) was used with this MCP detector.

Initial tests were done by placing the mass spectrometer in a vacuum chamber separate from the other parts of the instrument. The impact plate, made of tantalum, was coated with cesium iodide (CsI) salt. A 337 nm laser was fired at the plate through a window to generate ions. Ions were estimated to leave the impact plate with roughly 50 eV of kinetic energy.[95] A SIMION[64] simulation demonstrating how ions pass from the impact plate through the reflectron to the detector is given in Figure 16. The mass-to-charge ratio of ions only affects the flight time of the ions and does not affect their flight path. The path of the ions depends on the angle with which they leave the impact plate. As indicated, ions leaving the impact plate at angles perpendicular or near-perpendicular to the plate do not reach the detector.

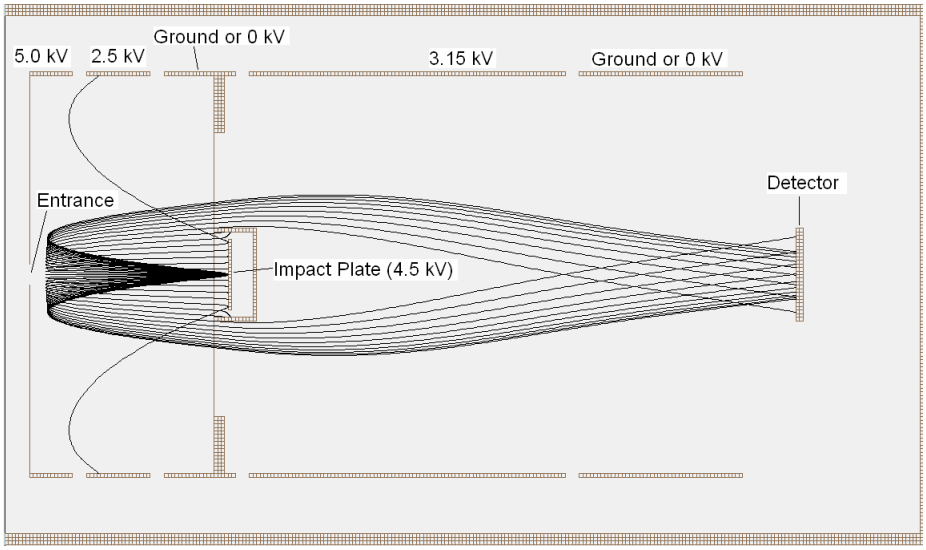

Figure 16. SIMION simulation of laser generated ions in the reflectron.

An example signal is given in Figure 17. As indicated, the amplitude of the signal is negative. The large peak near time zero is electrical noise from the laser pulse and indicated time zero.

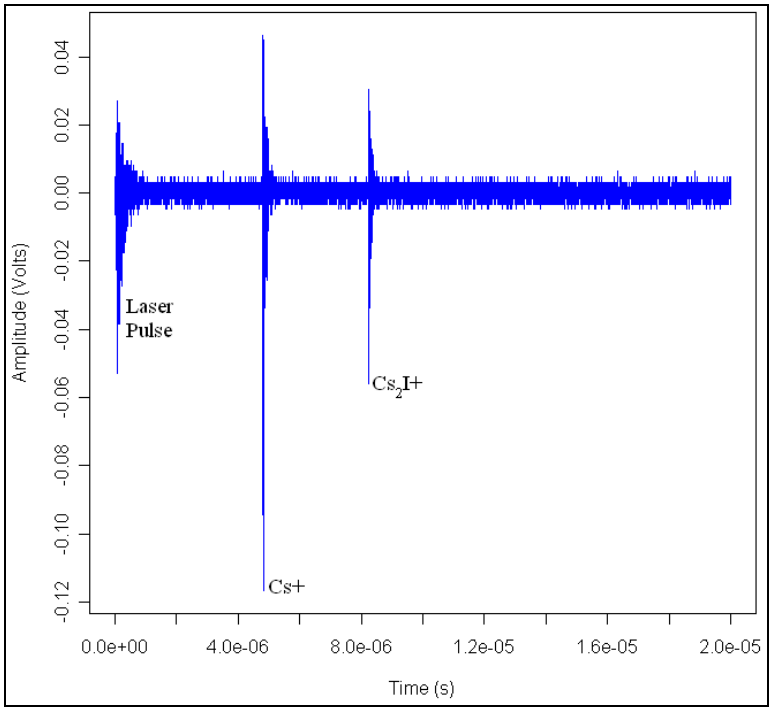

Figure 17. Example MCP signal obtained with the reflectron.

Figure 18 is the mass spectrum obtained by inverting the signal and converting the x-axis from flight time to mass-to-charge ratio using equation 2 given in section 1.3. As indicated, not all of the Cs^+, Cs_2^+ and Cs_2I^+ ions were observed in every signal. A histogram showing frequencies of observed peaks from 300 spectra is presented in Figure 19. As expected, the most frequently observed peak is from Cs^+; the Cs_2^+ peak is less frequent; and the Cs_2I^+ peak is observed the least.

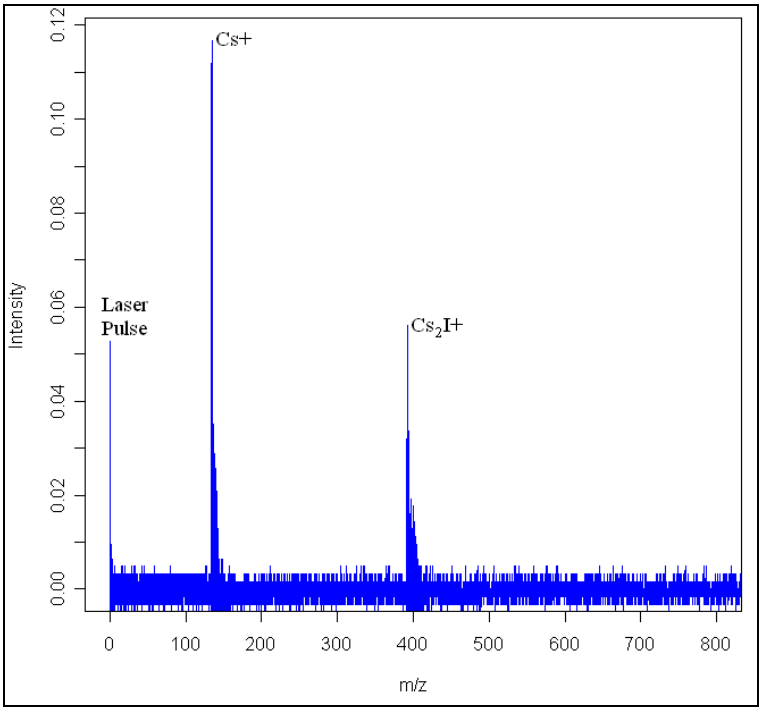

Figure 18. Example CsI mass spectrum obtained with the reflectron.

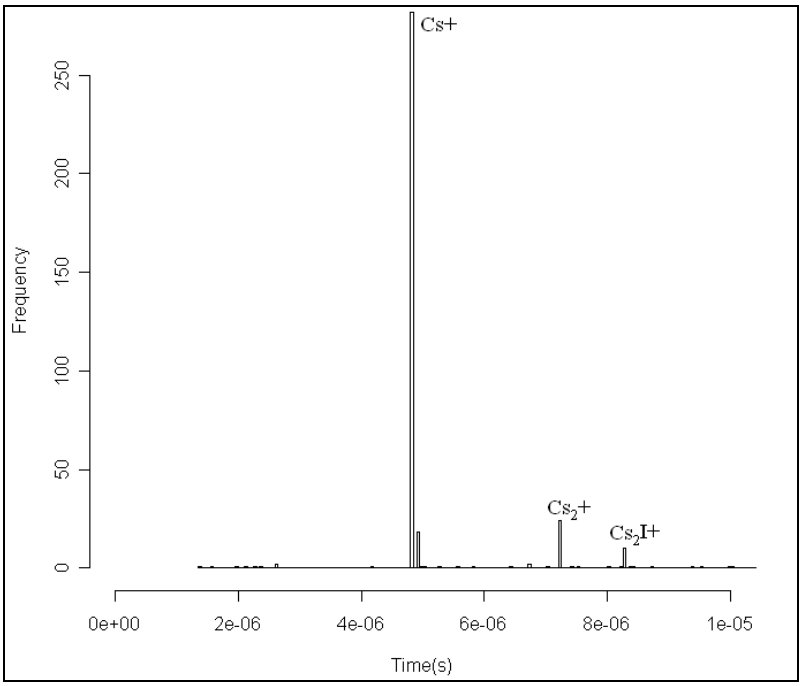

Figure 19. Histogram from 300 CsI spectra obtained with the reflectron.

The measured flight times were compared with calculated flight times obtained using SIMION.[64] These are presented in Table 3.

Table 3. Calculated and measured flight times for the reflectron.

	Cs^+	Cs_2^+	Cs_2I^+	Cs_2^+/Cs^+ Ratio	Cs_2I^+/Cs^+ Ratio
Exact Mass (amu):	132.905	265.811	392.715	-	-
SIMION Calculated Flight Time (μs):	4.708	6.657	8.092	1.414	1.719
Measured Flight Time (μs):	4.825	7.215	8.255	1.495	1.711

Observed flight times are slightly greater than expected from calculations. One contributing factor is imperfections in machining and/or measurements of machined parts. Another may be that calculated flight times were obtained from ions leaving the impact plate at a single angle with exactly 50 eV of energy, which may not accurately reflect the experiment. In reality, particles will leave with some distribution of kinetic energies and a variety of angles, causing deviation from the expected flight times.

Unshielded wires running to high voltage components could also introduce anomalies in flight times.

Another difficulty was impedance ringing observed in the signal. For example, the enlarging Cs^+ peak from Figure 17 is given below in Figure 20. This impedance ringing was reduced by modifying the lengths of cables between the MCP detector and amplifier, though some ringing was still present.

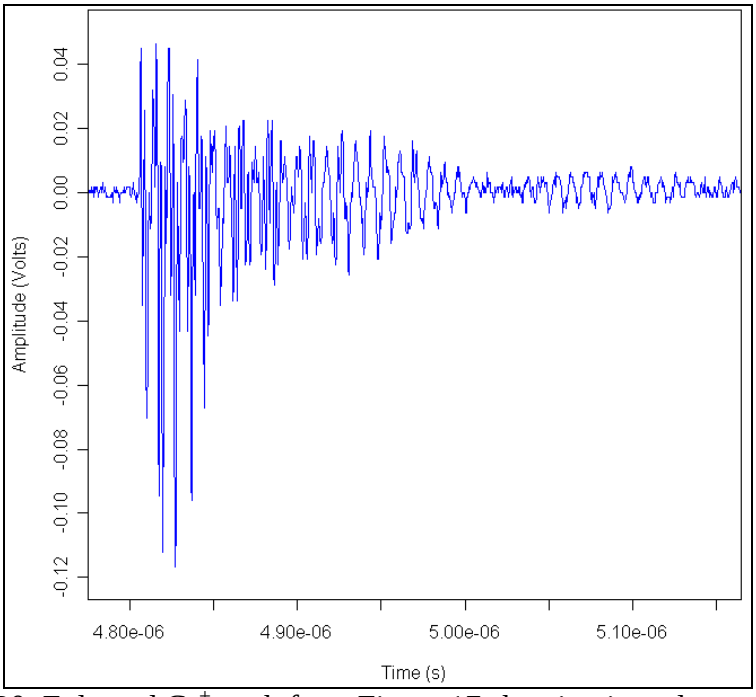

Figure 20. Enlarged Cs^+ peak from Figure 17 showing impedance ringing.

Ions generated when electrosprayed particles hit the impact plate have about 1–2 eV of energy when they leave the plate.[37] A simulation of the flight path of these ions shows that they are not able to reach the detector. Instead they follow a path similar to the ions in Figure 16 that leave the impact plate at an angle perpendicular to the plate.

As a result of this design flaw, a second mass spectrometer setup was created as depicted in Figure 21. This setup consisted of an impact plate and an Einzel lens to focus

particles. The Einzel lens had three cylinders with the middle cylinder at about 2 kV and the two outside cylinders at ground. To achieve improved resolution, this setup required a longer distance between the impact plate and the detector compared to the reflectron. This setup was also tested with the laser and yielded results similar to those obtained with the first or reflectron setup.

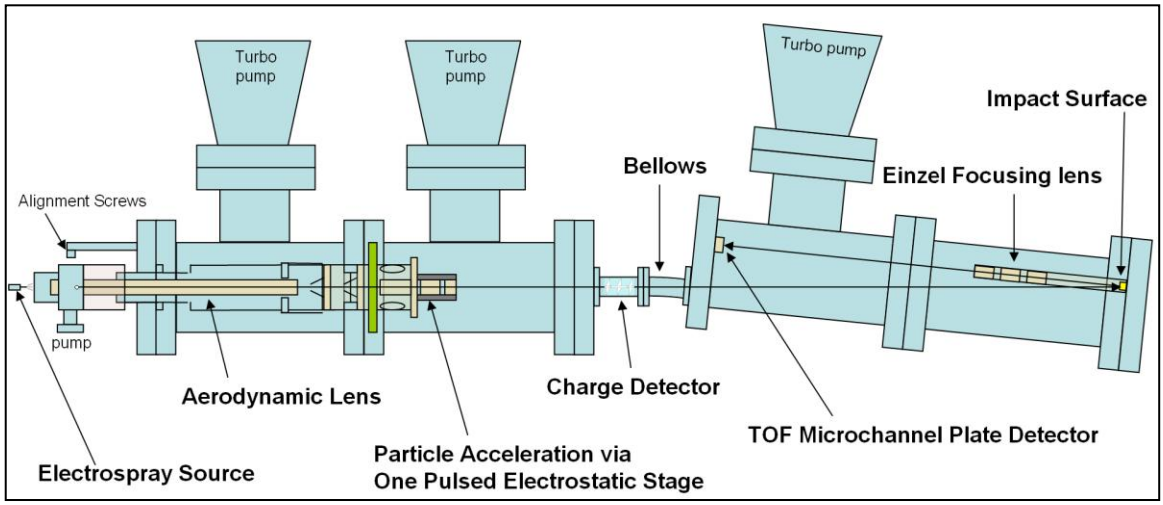

Figure 21. Second mass spectrometer setup.

Proper alignment with this system required many manual adjustments since the second half of the instrument was positioned at an angle relative to the first half. While tests with the laser were successful, alignment issues prevented this mass spectrometer from being used successfully with the electrospray. While the impact plate could be easily aligned with the electrospray particle beam, it was not possible to align the particle beam to prevent particles from hitting the Einzel lens before reaching the impact plate.

A solution to the problem with the first mass spectrometer was discovered, however. Since in this mass spectrometer, ions leaving the impact plate with 1–2 eV of energy were not able to reach the detector but again collided with the surface, the impact

plate was tilted at an angle of about 10 degrees. SIMION simulations[64] as displayed in Figure 22 show that ions leaving the impact plate with 1 eV always reach the detector, no matter the angle with which they leave the plate.

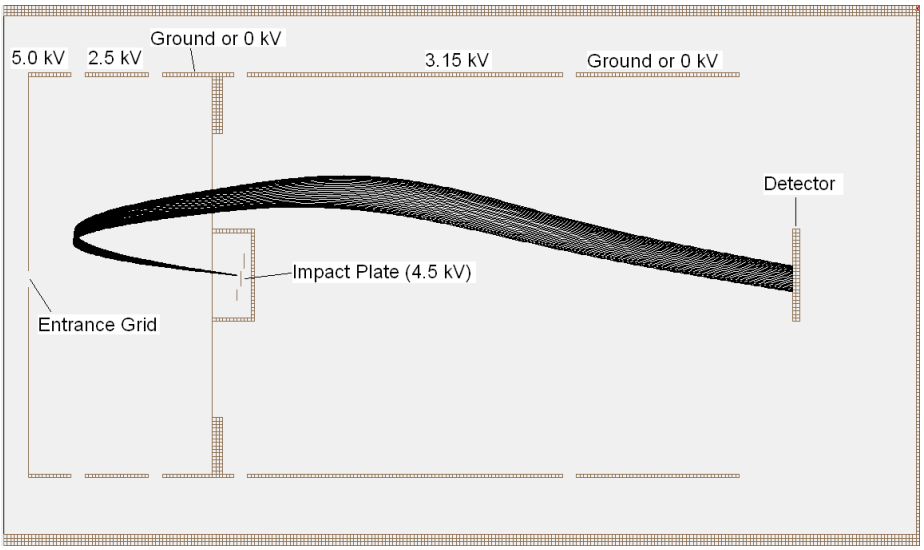

Figure 22. SIMION simulation of ions with 1 eV passing from a tilted impact plate to the detector in the reflectron mass spectrometer.

Another improvement to the mass spectrometer design included the use of better surfaces. In addition to a conductive diamond surface, fluorinated self-assembled monolayer (SAM) surfaces were prepared according to a well-established procedure.[4] Specifically, these were prepared by depositing a 200nm layer of gold on clean 0.25×0.25 inch silicon wafers. These gold wafers were cleaned in a Harrick plasma cleaner for 1 minute and immersed in 1mM solution of 1H,1H,2H,2H-perfluorododecane-1-thiol in 200 proof ethanol for 24 hours in the dark. As a control, a plasma cleaned gold wafer was immersed in ethanol under the same conditions. The quality of the surfaces was observed by measuring the contact angle of a distilled water

droplet on each surface. Measured angles were in the range of 116–119˚ which is in close agreement with the expected contact angle of 117˚.[5]

CHAPTER 4

RESULTS AND CONCLUSION

4.1 Results

All of the instrument's major components have been developed, including the electrospray source, aerodynamic lens, accelerator, image charge detector, impact surface, and MCP reflectron mass spectrometer. Four different types of electrospray capillaries were constructed including stainless steel, fused silica, nickel-cobalt, and filling needle capillaries. Two different desolvation techniques were employed including a heated capillary, and heated N_2 desolvating gas. This electrospray setup is capable of spraying both non-biological and biological samples including viruses.

The aerodynamic lens was successfully designed and tested, with electrosprayed particles observed passing through the lens. Alignment of the aerodynamic lens with the two skimmers and accelerator was successful, as determined by visual inspection with the LED light and by observing electrosprayed particles hitting the Faraday detector. The accelerator was also developed by adding grids on the high voltage and ground cylinders, allowing even poorly-centered particles to be accelerated.

The image charge detector measured the velocity, mass, and charge of electrosprayed particles after they passed through the aerodynamic lens and accelerator. Most of the noise from the accelerator was removed, and the noise from the turbo pumps was significantly reduced. The newest copper casing for the image charge detector was finished although time has not permitted a complete test from being performed. Future work should involve testing the performance of this new detector.

Both mass spectrometer setups were successfully tested with the laser using a CsI coated impact plate. Simulations of the reflectron mass spectrometer with a tilted impact plate show that product ions from electrosprayed particles successfully reach the detector, independent of the direction from which they leave the impact plate. Time limitations have prevented experiments with the tilted impact plate from being performed. Future work should involve testing this mass spectrometer setup with the new charge detector.

Testing was done with the second mass spectrometer setup with electrospray using a concentrated ammonium acetate solution in a 4:1 methanol, water mixture at pH 3.9 to see if a signal could be observed. Triggering with the image charge detector signal and looking for a mass spectrum at the time when samples were expected to reach the impact plate seemed to work well. Particles hitting the Einzel lens prevented a mass spectrum from being observed with this setup, though the reflectron mass spectrometer setup should produce a mass spectrum with a tilted impact plate. Since a mass spectrum has not been observed with the electrospray using a concentrated ammonium acetate solution, no attempt has yet been made to electrospray viruses. Suitable virus samples were obtained, however, and future work should involve tests with real viruses.

4.2 Conclusion

While time constraints prevented some components of the instrument from being completed, this research represents an important foundation on which exiting future work may be based. Currently, there is no automated, sensitive technique that will detect any known virus accurately and quickly. This technique is a fast, automated method that has the potential to do this. It is an automated technique, which in theory could detect a virus

with only a few virus particles present. The speed of detection is only limited by the fluid pumping speed and the size of the sample. The use of capsid structural information makes this technique very accurate. While virus mutations are frequent, these typically do not significantly change the masses of capsid proteins, making this technique very robust.

Appendix

Aerodynamic Lens Dimensions

The input parameters used by the lens calculator for designing the aerodynamic lens are given in Table 4. With these, the lens calculator produced the lens dimensions in Table 5 which were modified slightly to simplify machining. The lens calculator does not specify the inner diameter(d_t) or length(L_t) of the acceleration nozzle, though the lens calculator article[99] recommends using $d_t = 2d_n$ and $L_t = d_s$, where d_n is the inner diameter of the last lens and d_s is the spacer inner diameter. A better design for smaller particles is given in the literature.[56]

Table 4. Design input parameters for the aerodynamic lens calculator.

Properties of Carrier Gas (Air)		**Lens Conditions**	
Mass	28.964 g/mol	Number of lens elements (n) (excludes inlet and outlet orifices)	5
Specific heat ratio	1.4	Pressure before inlet	644.38 torr (85,910 Pa)
Viscosity	1.83×10^{-5} Pa s	Pressure before nozzle (optional)	(not specified)
Sutherland constant	110.4 K	Pressure after nozzle	0.20252 torr (27 Pa)
Mean free path	67.4 nm	Volumetric flow rate	0.1 slm
Particle Properties		Operating temperature	300 K
Density	1,300kg/m^3 or 1.3 g/cm^3	Detector distance	20 mm
Diameter range	38-500 nm		

Table 5. Lens dimensions in inches produced by the aerodynamic lens calculator.

Lens Number	Diameter	Modified Diameter	Spacer Length	Modified Spacer Length
0	0.005	0.005	2.528	2.750
1	0.146	0.147	1.620	1.600
2	0.136	0.136	1.715	1.700
3	0.124	0.120	1.853	1.850
4	0.108	0.106	2.097	2.100
5	0.073	0.073	2.955	2.950
6	0.097	0.096	NA	NA
Spacer Inner Diameter			0.584	
Modified Spacer Inner Diameter			0.750	
Accelerating Nozzle Length			0.584	
Modified Accelerating Nozzle Length			0.900	
Accelerating Nozzle Inner Diameter			0.194	
Modified Accelerating Nozzle Inner Diameter			0.192	

The lens calculator has a design and a test mode. After the parameters in Table A.2 were used to design the aerodynamic lens, the design modified for machining was tested using particles having a wide range of densities and diameters. The results are presented in Figures 23, 24, and 25.

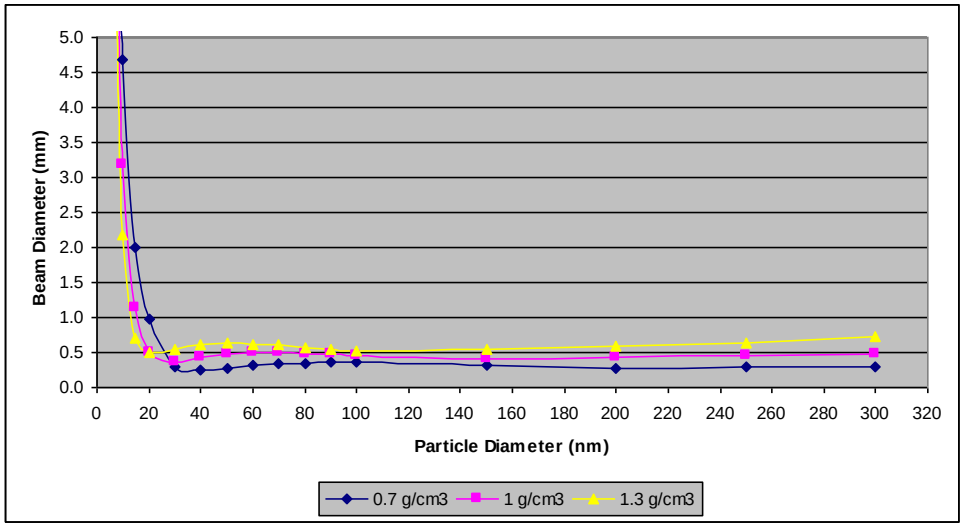

Figure 23. Estimated beam diameters for the aerodynamic lens.

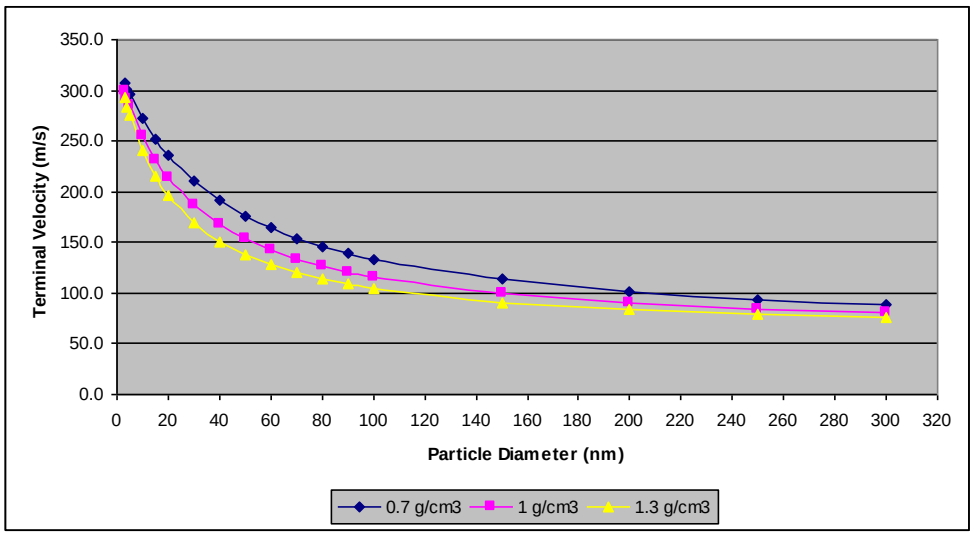

Figure 24. Estimated terminal velocities for the aerodynamic lens.

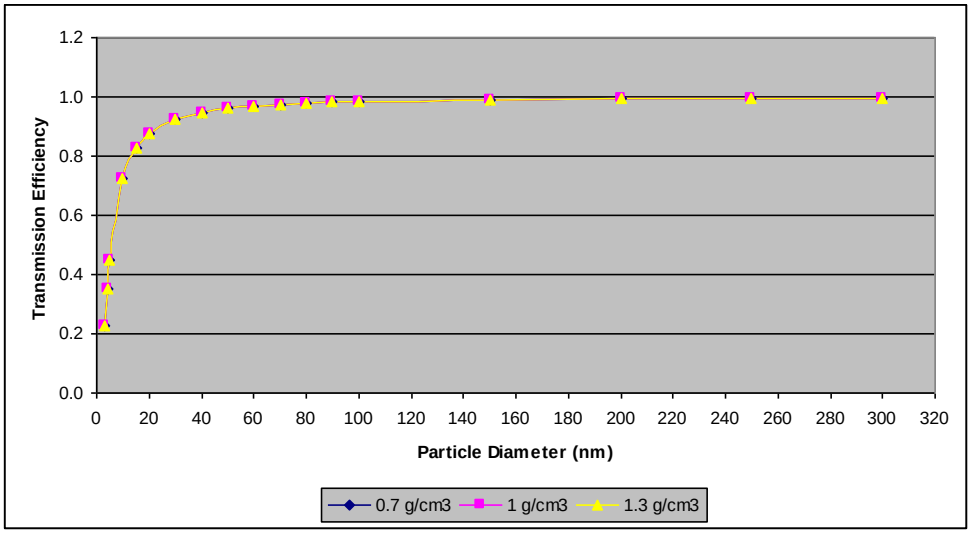

Figure 25. Estimated transmission efficiencies for the aerodynamic lens.

References

[1] Aksyonov, S. A.; Williams, P. Impact Desolvation of Electrosprayed Microdroplets – a New Ionization Method for Mass Spectrometry of Large Biomolecules. *Rapid Commun. Mass Spectrom.* **2001**, *15*, 2001–2006.

[2] Amptek A250 Application Notes. http://www.amptek.com/a250ap.html (accessed July 18, 2009), AN250-2, Rev. 3.

[3] Armed Forces International. http://www.armedforces-int.com/categories/the-need-for-biodetection/realtime-biological-agent-detection-particle-size-shape-fluorescence-characterisation.asp (accessed July 15, 2009). Article title: Real-Time Biological Agent Detection Using Particle Size, Shape and Fluorescence Characterization.

[4] Asemblon.com. http://www.asemblon.com/system/files/Self-Assembly+Procedure.pdf (Accessed July 21, 2009. Title: Asemblon, Inc. Self-Assembling Molecules.

[5] Asemblon.com. http://asemblon.com/content/1h1h2h2h-perfluorododecane-1-thiol (Accessed July 21, 2009. Title: 1H,1H,2H,2H-Perfluorododecane-1-thiol.

[6] Ast, T.; Riederer, D. E.; Miller, S. A.; Morris, M.; Cooks, R. G. Collisions of Fluorocarbon Ions at Solid Surfaces: Electronic Excitation, Surface-Induced Dissociation and Chemical Sputtering. *Org. Mass Spectrom.* **1993**, *28*, 1021–1033.

[7] Austin, D. E.; Beauchamp, J. L.; Manning, H. L. K.; Bailey, C. L. A Compact Time-of-Flight Mass Spectrometer for High-Flux Cosmic Dust Analysis. *J. Geophys. Res.* **2004**, *109*, E07S07.1–E07S07.5.

[8] Badman, E. R.; Johnson, R. C.; Plass, W. R.; Cooks, R. G. A Miniature Cylindrical Quadrupole Ion Trap: Simulation and Experiment. *Anal. Chem.* **1998**, *70*, 4896–4901.

[9] Baker, B. M.; Murphy, K. P. Prediction of Binding Energetics from Structure using Empirical Parameterization. *Methods Enzymol.* **1998**, *295*, 294–315.

[10] Barnes, J. H.; Hieftje, G. M.; Denton, M. B.; Sperline, R.; Koppenaal, D. W.; Barinaga, C. A. Mass Spectrometry Detector Array that Provides Truly Simultaneous Detection. *Am. Lab.* **2003**, *35*(20), 15–22.

[11] Benner, W. H. A Gated Electrostatic Ion Trap To Repetitiously Measure the Charge and m/z of Large Electrospray Ions. *Anal. Chem.* **1997,** *69*, 4162–4168.

[12] Bier, M. E.; Amy, J. W.; Cooks, R. G. Syka, J. E. P.; Ceja, P.; Stafford, G. A. Tandem Quadrupole Mass Spectrometer for the Study of Surface-Induced Dissociation. *Int. J. Mass Spectrom. Ion Processes*. **1987**, *77*, 31–47.

[13] Bothner, B.; Siuzdak, G. Electrospray Ionization of a Whole Virus: Analyzing Mass, Structure, and Viability. *ChemBioChem*. **2004**, *5*, 258–260.

[14] Bryden, W. A.; Benson, R. C.; Ecelberger, S. A.; Phillips, T. E.; Cotter, R. J.; Fenselau, C. The Tiny-TOF Mass Spectrometer for Chemical and Biological Sensing. *Johns Hopkins APL Technol. Dig.* **1995**, *16*, 296–310.

[15] Burgoyne, T. W.; Hieftje, G. M. An Introduction to Ion Optics for the Mass Spectrograph. *Mass Spectrom. Rev.* **1998**, *15*(4), 241–259.

[16] Burroughs, J. A.; Wainhaus, S. B.; Hanley, L. Impulsive Excitation of $Cr(CO)_6^+$ during Surface-Induced Dissociation at Organic Monolayers. *J. Phys. Chem.* **1994**, *98*, 10913–10919.

[17] Burroughs, J. A.; Wainhaus, S. B.; Hanley, L. Impulsive Excitation of $FeCp_2^+$ and $SiMe_3^+$ During Surface-Induced Dissociation at Organic Multilayers. *J. Chem. Phys.* **1995**, *103*(15), 6706–6715.

[18] Busch, K. L.; Glish, G. L.; McLuckey, S. A. *Mass spectrometry/mass spectrometry: techniques and applications of tandem mass spectrometry*; VCH Publishers: New York, N.Y, 1988.

[19] Cai, Y.; Peng, W. P.; Kuo, S. J.; Lee, Y. T.; Chang, H. C. Single-Particle Mass Spectrometry of Polystyrene Microspheres and Diamond Nanocrystals. *Anal. Chem.* **2002**, *74*(1), 232–238.

[20] Ceres, P.; Zlotnick, A. Weak Protein-Protein Interactions Are Sufficient To Drive Assembly of Hepatitis B Virus Capsids. *Biochemistry* **2002,** *41*, 11525–11531.

[21] Chorush, R. A.; Little, D. P.; Beu, S. C.; Wood, T. D.; McLafferty, F. W. Surface-Induced Dissociation of Multiply-Protonated Proteins. *Anal. Chem.* **1995,** *67*, 1042–1046.

[22] Mahy, B. W. (Author); Collier, L. (Editor); Balows, A. (Editor); Sussman, M. (Editor). *Topley and Wilson's Microbiology and Microbial Infections: Volume 1: Virology*, 9 ed.; Topley & Wilson's Microbiology & Microbial Infections: Dimmock, N.J., 1998.

[23] Cole, R. B. *Electrospray Ionization Mass Spectrometry: Fundamentals, Instrumentation, and Applications*; John Wiley & Sons: New York, NY, 1997, pp. 9, 15, 25.

[24] Cooks, R. G.; Ast, T.; Pradeep, T.; Wysocki V. Reactions of Ions with Organic Surfaces. *Acc. Chem. Res.* **1994**, *27*, 316–323.

[25] da Poian, A. T.; Oliveira, A. C.; Silva, J. L. Cold Denaturation of an Icosahedral virus. The Role of Entropy in Virus Assembly. *Biochemistry.* **1995**, *34*, 2672–2677.

[26] Dass, C. *Fundamentals of Contemporary Mass Spectrometry*, 1st ed; Wiley-Interscience: Hoboken, NJ, 2007.

[27] Despeymux, D.; Phillpotts, R.; Watts, P. Electrospray Mass Spectrometry for Detection and Characterization of Purified Cricket Paralysis Virus (CrPV). *Rapid Commun. Mass Spectrom.* **1996**, *10*, 937–941.

[28] Dole M.; Mack L. L.; Hines R. L.; Mobley R. C.; Ferguson L. D.; Alice M. B. (1968). Molecular Beams of Macroions. *J. Chem. Phys.* **49** (5): 2240–2249.

[29] Dongre, A. R.; Somogyit, A.; Wysocki, V. H. Surface-Induced Dissociation: An Effective Tool to Probe Structure, Energetics and Fragmentation Mechanisms of Protonated Peptides. *J. Mass Spectrom.* **1996**, *31*, 339–350.

[30] Dubois, F.; Knochenmuss, R.; Zenobi, R.; Brunelle, A.; Deprun, C.; Beyec, Y. L. A Comparison Between Ion-to-Photon and Microchannel Plate Detectors. *Rapid Commun. Mass Spectrom.* **1999**, *13*(9), 786–791.

[31] Ecelberger, S. A.; Cotter, R. J.; Cornish, T. J.; Fenselau, C.; Bryden, W. A. Proceedings of the 45th ASMS Conference on Mass Spectrometry and Allied Topics, Palm Springs, CA, 1997; p 469.

[32] Ferran, R. J.; Boumsellek, S. High-Pressure Effects in Miniature Arrays of Quadrupole Analyzers for Residual Gas Analysis from 10-9 to 10-2 Torr. *J. Vac. Sci. Technol., A* **1996**, *14*, 1258–1265.

[33] Fuerstenau, S. D.; Benner, W. H. Molecular Weight Determination of Megadalton DNA Electrospray Ions Using Charge Detection Time-of-flight Mass Spectrometry. *Rapid Communications in Mass Spectrometry*, **1995**, *9*, 1528–1538.

[34] Fuerstenau, S. D.; Benner, W. H.; Thomas, J. J.; Brugidou, C.; Bothner, B.; Siuzdak, G. Mass Spectrometry of an Intact Virus. *Angew. Chem. Int. Ed.*, **2001**, *40*(3), 541–544.

[35] Fuerstenau, S. D. Whole Virus Mass Analysis by Electrospray Ionization. *J. Mass Spectrom. Soc. Jpn.* **2003**, *51*(1), 50–53.

[36] Gatlin, C. L.; Turecek, F. Acidity Determination in Droplets Formed by Electrospraying Methanol-Water Solutions. *Anal. Chem.* **1994**, *66*, 712–718.

[37] Grill, V.; Shen, J.; Evans, C.; Cooks, R. G. Collisions of Ions with Surfaces at Chemically Relevant Energies: Instrumentation and Phenomena. *Rev. Sci. Instrum.* **2001**, *72*(8), 3149–3179.

[38] Harbeck, R. J.; Teague, J.; Crossen, G. R.; Maul, D. M.; Childers, P. L. Novel, Rapid Optical Immunoassay Technique for Detection of Group A Streptococci from Pharyngeal Specimens: Comparison with Standard Culture Methods. *J. Clin. Microbiol.*, **1993**, *31*(4), 839–844.

[39] Gupta, A.; Akin, D.; Bashir, R. Single Virus Particle Mass Detection using Microresonators with Nanoscale Thickness. *Appl. Phys. Lett.* **2004**, *84*(11), 1976–1978.

[40] Incardona, N. L. Encyclopedia of Life Sciences. http://mrw.interscience.wiley.com/emrw/9780470015902/els/article/a0000781/current/pdf (accessed Mar 14, 2008). Article title: Microviruses, 2001.

[41] Iribarne, J. V.; Thomson, B. A. On the Evaporation of Small Ions from Charged Droplets. *J. Chem. Phys.* **1976**, *64*(6): 2287–2294.

[42] Jacobs, D. C. The Role of Internal Energy and Approach Geometry in Molecule/Surface Reactive Scattering. *Condens. Matter.* **1995**, *7*, 1023–1045.

[43] Kane, T. E.; Somogyi, A.; Wysocki, V. H. Reactive Ion-Surface Collisions: Application of Ionized Acetone-d6, DMSO-d6 and Pyridine-d5 as Probes for the Characterization of Self-Assembled Monolayer Films on Gold. *Org. Mass Spectrom.* **1993**, *28*(12), 1665–1673.

[44] Kebarle, P. A Brief Overview of the Present Status of the Mechanisms Involved in Electrospray Mass Spectrometry. *J. Mass Spectrom.* **2000**, *35*, 804–817.

[45] Kebarle, P.; Tang, L. From Ions in Solution to Ions in the Gas Phase - the Mechanism of Electrospray Mass Spectrometry. *Anal. Chem.* **1993**, *65*, 972A–986A.

[46] Kelly, R. T.; Page, J. S.; Luo, Q.; Moore, R. J.; Orton, D. J.; Tang, K.; Smith, R. D. Chemically Etched Open Tubular and MonolithicEmitters for Nanoelectrospray Ionization Mass Spectrometry. *Anal. Chem.* **2006,** *78*, 7796–7801.

[47] King, R.; Bonfiglio, R.; Fernandez-Metzler, C.; Miller-Stein, C.; Olah, T. Mechanistic Investigation of Ionization Suppression in Electrospray Ionization. *J. Am. Soc. Mass Spectrom.* **2000**, *11*, 942–950.

[48] Kimmel, G. A.; Goodstein, D. M.; Levine, Z. H.; Cooper, B. H. Local Adsorbate-Induced Effects on Dynamical Charge Transfer in Ion-Surface Interactions. *Phys. Rev. B: Condens. Matter.* **1991**, *43*, 9403–9412.

[49] Knight, R. D. *Physics for Scientists and Engineers: A Strategic Approach*, Extended Ed. with MasteringPhysics; Addison Wesley: San Francisco, CA, 2004; pp 910–913.

[50] Kogan, V. T.; Kazanskii, A. D.; Pavlov, A. K.; Tubol'tsev, Yu. V.; Chichagov, Yu. V.; Gladkov, G. Yu.; Illl'yasov, E. I. Portable Mass Spectrometer for Ecology Studies. *Instrum. Exp. Technol.-Engl. Tr.* **1995**, *38*, 106–110.

[51] Koppers, W. R.; Beijersbergen, J. H. M.; Weeding, T. L.; Kistemaker, P. G.; Kleyn, A. W. Dissociative Scattering of CF^{+}_{3} from a barium-covered Ag(111) Surface. *Surf. Sci.* **1996**, *358*, 678–683.

[52] Koppers, W. R.; Gleeson, M. A.; Lourenco, J.; Weeding, T. L.; Los, J.; Kleyn, A. W. Dissociative Scattering of Fluorocarbon Ions from a Liquid Surface at Hyperthermal Incident Energies. *J. Chem. Phys.* **1999**, *110*, 2588–2596.

[53] Laprade, B. N.; Labich, R. J. Microchannel Plate-Based Detectors in Mass Spectrometry. *Spectroscopy*. **1994**. *9*(5), 26–30.

[54] Laskin, J; Futrell, J. H. Activation of Large Ions in FT-ICR Mass Spectrometry. *Mass Spectrom. Rev.* **2005**, *24*(2), 135–167.

[55] Leland, D. S.; Ginocchio, C. C. Role of Cell Culture for Virus Detection in the Age of Technology. *Clin. Microbiol. Rev.* **2007**, *20*, 49–78.

[56] Liu, P.; Ziemann, P. J.; Kittelson, D. B.; McMurry, P. H. Generating Particle Beams of Controlled Dimensions and Divergence: I. Theory of Particle Motion in Aerodynamic Lenses and Nozzle Expansions. *Aerosol Sci. Technol.* **1995**, *22*(3), 293–313.

[57] Liu, P.; Ziemann, P. J.; Kittelson, D. B.; McMurry, P. H. Generating Particle Beams of Controlled Dimensions and Divergence: II. Experimental Evaluation of Particle Motion in Aerodynamic Lenses and Nozzle Expansions. *Aerosol Sci. Technol.* **1995**, *22*(3), 314–324.

[58] Loo, J. A.; Holler, T. P.; Foltin, S. K.; McConnell, P.; Banotai, C. A.; Horne, W.; Mueller, T.; Stevenson, T. I.; Mack, D. P. Application of Electrospray Ionization Mass Spectrometry for Studying Human Immunodeficiency Virus Protein Complexes. *Proteins Struct. Funct. Genet.* **1998**, *2*, 28–37.

[59] Mabbett, S. R.; Zilch, L. W.; Maze, J. T.; Smith, J. W.; Jarrold, M. F. Pulsed Acceleration Charge Detection Mass Spectrometry: Application to Weighing Electrosprayed Droplets. *Anal. Chem.* **2007**, *79*(22), 8431–8439.

[60] Mamyrin, B. A.; Karataev, V. I.; Shmikk, D. V.; Zagulin, V. A. The Mass-Reflectron, a New Nonmagnetic Time-of-Flight Mass Spectrometer with High Resolution. *Sov. Phys. JETP*, **1973**, *37*, 45.

[61] Mamyrin, B.A. Time-of-Flight Mass Spectrometry (Concepts, Achievements, and Prospects). *Int. J. Mass spectrom.* **2001**, *206*, 251–266.

[62] Mann, M. Electrospray: Its Potential and Limitations as an Ionization Method for Biomolecules. *Org. Mass Spectrom.* **1990**, *25*(11), 575–587.

[63] Mass Spectrometers. *Encyclopedia of Applied Physics*, G. L. Trigg Ed.; VCH Publishers: New York, 1997; Vol. 19, p. 289.

[64] Mass Spectrometry Software from Scientific Instrument Services, Inc. http://www.sisweb.com/software.htm (accessed August 6, 2009), Ringoes, NJ.

[65] Mavromoustakis, C. T.; Witiak, D. T.; Hughes, J. H.. Effect of High-Speed Rolling on Herpes Simplex Virus Detection and Replication. *J. Clin. Microbiol.* **1988**, *26*, 2328–2331.

[66] Maze, J. T.; Jones, T. C.; Jarrold, M. F. Negative Droplets from Positive Electrospray. *J. Phys. Chem. A.* **2006,** *110*, 12607–12612.

[67] McLuckey, S. A.; Stephenson, J. L. Ion/Ion Chemistry of High-Mass Multiply Charged Ions. *Mass Spectrom. Rev.* **1998**, *17*(6), 369–407.

[68] Miller, G.; Koch, M.; Hsu, J. P.; Ozuna, F. *Proceedings of the 45th ASMS Conference on Mass Spectrometry and Allied Topics*, Palm Springs, CA, 1997; p 1163.

[69] Mizogawa, T.; Shiromarub, H.; Satoc, M.; Ito, Y. A Two-Dimensional Position-Sensitive Ion Detector Based on Modified Backgammon Method with Weighted-Coupling Capacitors. *Int. J. Mass spectrom.* **2002**, *215*, 141–149.

[70] Mørtz, E; O'Connor, P. B.; Roepstorff, P.; Kelleher, N. L.; Wood, T. D.; McLafferty, F. W.; Mann, M. Sequence Tag Identification of Intact Proteins by Matching Tandem Mass Spectral Data Against Sequence Data Bases. *Proc. Natl. Acad. Sci. U. S. A.* **1996**, *93*(16): 8264–8267.

[71] Orient, O. J.; Chutjian, A.; Garkanian, V. Miniature, High-Resolution, Quadrupole Mass-Spectrometer Array. *Rev. Sci. Instrum.* **1997**, *68*(3), 1393–1397.

[72] Paya, C. V.; Wald, A. D.; Smith, T. F. Detection of Cytomegalovirus Infections in Specimens other than Urine by the Shell Vial Assay and Conventional Tube Cell Cultures. J. Clin. Microbiol. **1987**, *25*, 755–757.

[73] Peter-Katalinic, J.; Hillenkamp, F. *MALDI MS: A Practical Guide to Instrumentation, Methods and Applications;* Weinheim: Wiley-VCH, 2007.

[74] Practical Electromagnetic Shielding. http://www.cvel.clemson.edu/emc/tutorials/Shielding02/Practical_Shielding.html (Aug 1, 2009).

[75] Pradeep, T.; Ast, T.; Cooks, R. G.; Feng, B. Low-Energy Collisions of Group IIIA, IVA, VA, VIA, and VIIA Ions with Fluoroalkyl SAM Surfaces: Reactions, Chemical Sputtering, and Mechanistic Implications. *J. Phys. Chem.* **1994**, *98*, 9301–9311.

[76] Rakov, V. S.; Denisov, E. V.; Futrell, J. H.; Ridge, D. P. Surface Induced Dissociation of Chromium Hexacarbonyl on Fluorinated Alkanethiolate Surface in ion Cyclotron Resonance Mass Spectrometer: Studies of Energetics of the Process Using Recursive Internal Energy Distribution Search Method. *Int. J. Mass spectrom.* **2002**, *213*, 25–44.

[77] Schultz, J. C.; Hack, C. A.; Benner, W. H. Polymerase Chain Reaction Products Analyzed by Charge Detection Mass Spectrometry. *Rapid Commun. Mass Spectrom.* **1999**, *13*, 15–20.

[78] Schultz, D. G.; Hanley, L. Shattering of $SiMe^{3+}$ During Surface-Induced Dissociation. *J. Chem. Phys.* **1998**, *109*(24), 10976–10983.

[79] Schultz, J. C.; Hack, C. A.; Benner, W. H. Mass Determination of Megadalton-DNA Electrospray Ions Using Charge Detection Mass Spectrometry. *J. Am. Soc. Mass Spectrom.* **1998**, *9*, 305–313.

[80] Sinha, M. Presented at the *46th ASMS Conference on Mass Spectrometry and Allied Topics*, Orlando, FL, May 31–June 4, 1998.

[81] Sinha, M. P.; Tomassian, A. D. Development of a Miniaturized, Light-Weight Magnetic Sector for a Field-Portable Mass Spectrograph. *Rev. Sci. Instrum.* **1991**, *62*(11), 2618–2620.

[82] Siuzdakl, G.; Bothnet, B.; Yeager, M.; Brugidou, C.; Fauquet, C. M.; Hoey, K.; Chang, C. M. Mass Spectrometry and Viral Analysis. Chemistry and Biology. **1996**, *3*(1), 45–48.

[83] Sleno, L.; Volmer, D. A. Ion Activation Methods for Tandem Mass Spectrometry. *J. Mass Spectrom.* **2004**, *39*(10), 1091–112.

[84] Smith, C. E.; Lauffer, M. A. Polymerization-Depolymerization of Tobacco Mosaic Virus Protein. 8.

Lightscattering studies. *Biochemistry* **1967**, *6*, 2457–2464.

[85] Smith, J. N.; Flagan, R. C.; Beauchamp, J. L. Droplet Evaporation and Discharge Dynamics in Electrospray Ionization. *J. Phys. Chem. A* **2002,** *106*, 9957–9967.

[86] Somogyi, A.; Kane, T. E.; Ding, J. M.; Wysocki, V. H. Reactive Collisions of Benzene Ion $C_6H_6{\cdot}^+$ and $D_6H_6{\cdot}^+$ at Self-Assembled Monolayer Films Prepared on Gold from n-Alkane Thiols and a Fluorinated Alkanethiol: the Influence of Chain Length on the Reactivity of the Films and the Neutralization of the Projectile. *J. Am. Chem. Soc.* **1993**, *115*(12), 5275–5283.

[87] St. John, P. M.; Beck, R. D.; Whetten, R. L. Reactions in Cluster-Surface Collisions. *Phys. Rev. Lett.* **1992**, *69*(9), 1467–1470.

[88] St. John, P. M.; Yeretzian, C.; Whetten, R. L. Electron Emission Mechanism for Impact of Carbon (C_N-) and Silicon (Si_N-) Clusters. *J. Phys. Chem.* **1992**, *96*, 9100–9104.

[89] Stephen, D. F. Whole Virus Mass Analysis by Electrospray Ionization. *J. Mass Spectrom. Soc. Jpn.* **2003**, *51*(1), 50–53.

[90] Swatkoski, S.; Russell, S.; Edwards, N.; Fenselau, C. Analysis of a Model Virus Using Residue-Specific Chemical Cleavage and MALDI-TOF Mass Spectrometry. *Anal. Chem.* **2007,** *79*, 654–658.

[91] Thomas, J. J.; Bothner, B.; Traina, J.; Benner, W. H.; Siuzdak, G. Electrospray Ion Mobility Spectrometry of Intact Viruses. *Spectroscopy (Amsterdam, Netherlands)*. **2004**, *18*(1), 31–36.

[92] Tito, M. A.; Tars, K.; Valegard, K.; Hajdu, J.; Robinson, C. V. Electrospray Time-of-Flight Mass Spectrometry of the Intact MS2 Virus Capsid. *J. Am. Chem. Soc.* **2000,** *122*, 3550–3551.

[93] Todd, J. F. J.; March, R. E. A Retrospective Review of the Development and Application of the Quadrupole Ion Trap Prior to the Appearance of Commercial Instruments *Int. J. Mass Spectrom.* **1999**, *9*, 190–191.

[94] Tong, X. C. *Advanced Materials and Design for Electromagnetic Interference Shielding*, Illustrated ed.; CRC Press: Boca Raton, FL, 2008; pp. 15–16.

[95] Torrisi, L.; Margarone, D.; Borrielli, A.; Caridi, F. Ion and Photon Emission from Laser-Generated Titanium-Plasma. *Appl. Surf. Sci.* **2008**, *254*, 4007–4012.

[96] Wainhaus, S. B.; Burroughs, J. A.; Hanley, L. Charge Transfer During Pyridine Ion Scattering Off Clean and Oxygen Modified Ni(111). *Surf. Sci.* **1995**, *344*, 122–130.

[97] Wang, X.; Kruis, F. E.; McMurry, P. H. Aerodynamic Focusing of Nanoparticles: I. Guidelines for Designing Aerodynamic Lenses for Nanoparticles. *Aerosol Sci. Technol.* **2005**, *39*(7), 611–623.

[98] Wang, X.; Gidwani, A.; Girshick, S. L.; McMurry, P. H. Aerodynamic Focusing of Nanoparticles: II. Numerical Simulation of Particle Motion Through Aerodynamic Lenses. *Aerosol Sci. Technol.* **2005**, *39*(7), 624–636.

[99] Wang, X.; McMurry, P. H. A Design Tool for Aerodynamic Lens Systems. *Aerosol Sci. Technol.* **2006**, *40*, 320–334.

[100] Wang, X.; McMurry, P. H. Instruction Manual for the Aerodynamic Lens Calculator. *Aerosol Sci. Technol.* **2006**, *40*, 1–10.

[101] Watzinger, F.; Suda, M.; Preuner, S.; Baumgartinger, R.; Ebner, K.; Baskova, L.; Niesters, H. G. M.; Lawitschka, A.; Lion, T. Real-Time Quantitative PCR Assays for Detection and Monitoring of

Pathogenic Human Viruses in Immunosuppressed Pediatric Patients. *J. Clin. Microbiol.* **2004**, *42*(11), 5189–5198.

[102] Wells, J. M.; McLuckey, S. A. Collision-Induced Dissociation (CID) of Peptides and Proteins. *Meth. Enzymol.* **2005,** *402*, 148–185.

[103] Wynne, S. A.; Crowther, R. A.; Leslie, A. G. W. The Crystal Structure of the Human Hepatitis B Virus Capsid. *Molecular Cell* **1999**, *3*, 771–780.

[104] Wysocki, V. H.; Joyce, K. E.; Jones, C. M.; Beardsley, R. L. Surface-Induced Dissociation of Small Molecules, Peptides, and Non-Covalent Protein Complexes. *J. Am. Soc. Mass. Spectrom.* **2008**, *19*, 190–208.

[105] Zhang, X.; Smith, K. A.; Worsnop, D. R.; Jimenez, J.; Jayne, J. T.; Kolb, C. E. A Numerical Characterization of Particle Beam Collimation by an Aerodynamic Lens-Nozzle System: Part I. An Individual Lens or Nozzle. *Aerosol Sci. Technol.* **2002**, *36*, 617–631.

[106] Zhang, X.; Smith, K. A.; Worsnop, D. R.; Jimenez, J.; Jayne, J. T.; Kolb, C. E.; Morris, J.; Davidovits, P. Numerical Characterization of Particle Beam Collimation: Part II. Integrated Aerodynamic-Lens-Nozzle System. *Aerosol Sci. Technol.* **2004**, *38*(6), 619–638.

[107] Ziegler, Z. Ion Traps Come of Age *Anal. Chem.* **2002**, *74*(17) 489A–492A.

[108] Zilch, L. W.; Maze, J. T.; Smith, J. W.; Edwin, G. E.; Jarrold, M. F. Charge Separation in the Aerodynamic Breakup of Micrometer-Sized Water Droplets. *J. Phys. Chem. A.* **2008,** *112*, 13352–13363.

[109] Zilch, L. W.; Maze, J. T.; Smith, J. W.; Jarrold, M. F. Freezing, Fragmentation, and Charge Separation in Sonic Sprayed Water Droplets. *Int. J. Mass spectrom.* **2009**, *283*, 191–199.